RESEARCH ARTICLE

Implementation of Traveling Wave Models of Grating-Based Integrated Optical Devices for Circuit Simulation

J. H. RASMUSSEN AND TOM J. SMY
Department of Electronics (DoE), Carleton University, Ottawa, ON K1S 5B6, Canada

Corresponding author: Tom J. Smy (tomsmy@cunet.carleton.ca)

ABSTRACT This paper presents the development and use of a traveling wave model of waveguide-based grating devices for use as a compact model in a circuit-level simulator. Both passive and active devices are modeled, with the grating being characterized by coupling coefficients for the two counter-propagating waves. It is shown how the implicit carrier frequency can be offset from the Bragg frequency using two possible methods: either by the static detuning of the model or introducing a phase modulation into the coupling coefficients. Other physical aspects of the model are addressed such as dispersion and energy conservation. A comparison to a 1D Yee-cell model is used to verify the applicability of the traveling wave model. As an example of the circuit simulation of a passive device, an optical code generating application is used and it is noted that for a passive device the interface between the compact model and the circuit simulator is not a concern. Using traveling-wave-based laser simulations of grating-based laser structures it is demonstrated that the model captures the complex behaviour of the devices. In particular the lasing frequency is naturally produced from the model and the introduction of delay elements into the structure can be used to restrict the laser to single mode operation. A number of examples are used to illustrate important aspects of its use as a compact model. Firstly, it is shown that an operating point for either of the laser configurations can be constructed and detuning used to produce an un-modulated output, allowing for much more efficient simulations. A final example uses a directly modulated laser to illustrate the effect of back reflection on the stability of the laser simulation.

INDEX TERMS Laser, modeling, traveling wave, photonic circuit analysis.

NOMENCLATURE
GLOSSARY
BC	Boundary Condition. 3.
DBR	Distributed Bragg Reflector. 2, 7, 8, 14-18, 21, 22.
DFB	Distributed Feedback Laser. 2, 7-9, 14-22.
FDTD	Finite Difference Time Domain. 2, 9, 10.
FFT	Fast Fourier Transform. 15.
FP	Fabry-Pérot. 2, 3, 5, 7-9, 13-15.
FSS	Fast Steady State. 5, 8, 9, 17, 18.
FTSS	Fine-Tuned Steady State. 5, 8, 9, 17, 18.
LNA	Low Noise Amplifier. 21.
MNA	Modified Nodal Analysis. 3-5.
NR	Newton-Raphson. 4, 5.
OP	Operating Point. 2, 5, 8, 9, 17, 18.
PD	Photo-Detector. 21.
PS	Pre-simulation. 5, 8, 9.
SPE	Spontaneous Emission. 3, 5, 16, 17.
SS	Steady State. 2, 5, 9, 15-17, 19, 21.
TWM	Traveling Wave Model. 2-15, 17-19, 21.

I. INTRODUCTION
The voluminous and ongoing work into photonics technologies and the wide spread application of such technologies, in areas such as sensors and communications, has lead to a significant demand for design tools that enable quick

efficient work flows. In particular the tight integration of electronics and photonics in circuits motivates the creation of circuit-level tools capable of self-consistently simulating mixed (electrical/optical) circuits and systems. This impetus has lead to work in both frequency and time domain methods, work into co-simulation of electronics and optical devices [1], [2], [3], [4], [5], as well as commercial efforts [6], [7], [8].

A key requirement of all such system-level simulators is quick efficient compact models of the elements of the circuit. Electrical components such as bipolar transistors have well established compact models for use in both the frequency and time-domains. Compact models for optical devices, however, are less well developed and present quite different challenges. In particular, the distributed nature of an optical device is often an important factor in the device operation. Phenomena such interference, dispersion, and the presence of modes can be key. A particularly useful approach for modeling waveguide-based devices in time-domain analysis is the use of a Traveling Wave Model (TWM). The model represents the optical signals as counter-propagating complex envelopes with the carrier removed. Such a representation is very advantageous for system-level simulation because the need to model the very fast modulation of the carrier is eliminated. The TWM model is remarkably flexible, enabling the modeling of passive and active devices from simple gratings to lasers. A large literature dealing with the application of the TWM to a wide range of structures with experimental verification is available [9], [10], [11], [12], [13].

The use of a TWM model in a fully integrated optical/electrical simulator, based on a spice-like configuration, was presented in [14]. This paper introduced the basic TWM compact model development and illustrated the use of the device with examples of passive and active devices used in mixed electrical/optical circuits. It is important that time-domain compact models have a means of predicting a steady-state (SS) solution to enable the system simulator to find an operating point (OP) of the circuit. This is a significant challenge for compact models of lasers as the they are characterized by a harmonic SS with stochastic variation and can produce chaotic behaviour [15]. However, a methodology to obtain an effective OP for a Fabry-Pérot (FP) laser has also been developed [16].

Optical technologies incorporating waveguides with incorporated gratings are very common [17], [18], [19], with a wide range of passive and active applications. Although TWM models have been widely used for grating-based optical devices [18], [20], [21], the use of a TWM compact model in a system/circuit-level simulator produces a number of issues that need to be addressed. Although initial work on simple grating-based passive devices was reported in [14], the modeling of the grating and the phenomena produced were not significantly explored as the emphasis was on the creation of the compact model and integration into the circuit simulator framework. A very important application of gratings is their use as a distributed mirror in active devices such as Distributed Bragg Reflector (DBR)-based lasers and

Distributed Feedback (DFB) lasers. Neither of these devices were dealt with in [14] or [16]. Although the fundamental principles on which these lasers are based is similar to FP lasers, in a number of aspects they are dissimilar and these differences have implications on the use of the TWM as a compact model. With respect to the work presented in [14] and [16], in this paper we will first deal more carefully and extensively with passive applications of gratings and then, importantly, will address the implications of grating based laser simulations, using TWM based models, within a circuit simulation framework.

Sec. II outlines the basic TWM model, presenting the optical field equations and a carrier equation for active devices. The second part of this section reviews the numerical implementation of the model as well as the integration into a circuit-level simulator. Sec. III reviews the important physical phenomena present in grating-based devices. Close attention is paid to modeling issues with a discussion of the model coupling coefficients, dispersion, and group velocity. To illuminate the physics of the grating and verify the appropriate use of the TWM model, a 1D Yee-cell-based finite difference time-domain (FDTD) model is used as a reference. The end of this section discusses the physics and model implementation of grating-based lasers. Finally, two sections (Sec. IV and Sec.V) will present a number of examples to illustrate the use of the compact model in a variety of configurations, including a passive optical code generator and a directly modulated DFB laser.

II. BASIC THEORY AND IMPLEMENTATION
This section will first outline the basic TWM model dealing with the field equations and the additional carrier equation needed to model optical amplifiers and lasers. The second section will outline the methodology used to create a compact model from the TWM for use in a circuit/system-level simulator.

A. TRAVELING WAVE MODEL
The derivation of the TWM model results from two basic assumptions: 1) propagation of the electromagnetic field in a homogeneous waveguide which is described by a set of transverse modes each with a specific group velocity v_g and effective index n_g and 2) identification of a reference (or carrier) wavelength associated with the field. Such a model is a good candidate for a compact model as it models the evolution of the envelope of the optical signal and not the fundamental frequency.

1) FIELD EQUATIONS
If we assume for simplicity that only one transverse mode is excited then the total field (which is the sum of two counter-propagating fields $\hat{E}_{fc}$ and $\hat{E}_{rc}$) in the waveguide is given by,

$$\begin{aligned}
\hat{E}(t, z) &= \hat{E}_{fc} + \hat{E}_{rc} \\
&= \hat{E}_f(t) e^{i(\omega_c t - k_c z)} + \hat{E}_r(t) e^{i(\omega_c t + k_c z)},
\end{aligned}$$
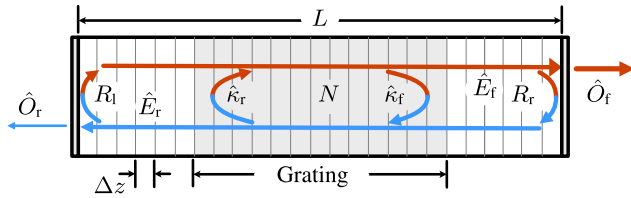
FIGURE 1. Waveguide/Laser geometry showing the length (L), width w and the three primary variables for the TWM: carrier density N and forward and reverse propagating complex fields $\hat{E}_f$ and $\hat{E}_r$. Also shown are facet/mirror reflectivities, the presence of grating region characterized by coupling coefficients $\hat{\kappa}_{f,r}$, and the optical outputs $\hat{O}_{f,r}$.

where $\hat{E}_f$ and $\hat{E}_r$ are complex envelopes for the forward and reverse propagating fields. These capture both the local magnitude and phase of the signals.[1] The carrier frequency and wavenumber for the signal are given by ω_c and k_c.

One of the advantages of the TWM is its physical nature and the ease with which phenomena can be added to the model. The propagation constant $\hat{\beta}$ can be used to model the local material gain, index variation due to the presence of carriers $N(z)$, or a static detuning of the carrier wavelength. In addition, and of particular importance for modeling grating-based devices, coupling between the forward and reverse traveling waves can be incorporated using the coupling coefficients $\hat{\kappa}_{f,r}$. Finally, spontaneous emission (SPE) can be modeled by adding stochastic terms to the equations ($\hat{F}_f$ and $\hat{F}_r$). With these additions the two 1st-order wave equations describing the evolution of these two signals are [9]:

$$\frac{1}{v_g}\frac{\partial \hat{E}_f}{\partial t} = -\frac{\partial \hat{E}_f}{\partial z} - i\hat{\beta}(N,S)\hat{E}_f + i\hat{\kappa}_f\hat{E}_r + \hat{F}_f \quad (1a)$$

$$\frac{1}{v_g}\frac{\partial \hat{E}_r}{\partial t} = +\frac{\partial \hat{E}_r}{\partial z} - i\hat{\beta}(N,S)\hat{E}_r + i\hat{\kappa}_r\hat{E}_f + \hat{F}_r, \quad (1b)$$

where v_g is the group velocity[2] of the propagating mode and $\hat{\beta}(N,S)$ defines a gain/loss term given by,

$$\hat{\beta}(N,S) = \frac{1}{2}\left[\delta + \alpha_H G_0(N,S) + ig_f G_0(N,S)\right], \quad (2)$$

where the parameter δ is a static detuning factor that determines the carrier frequency ω_c and the factors $\alpha_H G_0(N,S)$ and $g_f G(N,S)$ capture dynamic carrier induced detuning and gain respectively. The two coefficients $\hat{\kappa}_f$ and $\hat{\kappa}_r$ describe coupling of the two counter-propagating waves. We define a photon density $S(z) = |\hat{E}_f(z)|^2 + |\hat{E}_r(z)|^2$ where it is assumed that the two signals are normalized correctly. The set of equations in (1) are well suited for modeling both passive

waveguide-based devices and active devices such as optical amplifiers and lasers (see Fig. 1).

A TWM of a simple passive grating would drop the gain/loss and spontaneous emission terms, and conservation of energy requires we set $\hat{\kappa}_f = \hat{\kappa}_r^*$,[3] resulting in,

$$\frac{1}{v_g}\frac{\partial \hat{E}_f}{\partial t} = -\frac{\partial \hat{E}_f}{\partial z} - i\frac{\delta}{2}\hat{E}_f + i\hat{\kappa}_f\hat{E}_r \quad (3a)$$

$$\frac{1}{v_g}\frac{\partial \hat{E}_r}{\partial t} = +\frac{\partial \hat{E}_r}{\partial z} - i\frac{\delta}{2}\hat{E}_r + i\hat{\kappa}_f^*\hat{E}_f, \quad (3b)$$

where we have retained the static detuning terms.

2) LASER MODEL

To create a TWM model of a semiconductor laser a number of effects need to be added. First, the addition of a simple distributed rate equation of the excess carrier density ($N(z)$) is needed. The equation describing the evolution of the carrier density is given by a distributed 1st-order rate equation:

$$\frac{dN(z)}{dt} = \frac{\eta I_D}{qV_l} - G_0(N(z) - N_{tr})S(z) - \frac{N(z)}{\tau_n}, \quad (4)$$

where we have a differential gain G_0, η is the quantum efficiency, V_l the volume of the active region, I_D is the laser current and τ_n the spontaneous emission coefficient.

To complete a Fabry-Pérot (FP) laser model it should be noted that the presence of mirrors places a boundary condition (BC) on the two fields such that:

$$\hat{E}_f(0) = R\,\hat{E}_r(0) \;\; \text{and} \;\; \hat{E}_r(L) = R\,\hat{E}_f(L), \quad (5)$$

where R is the reflectivity of the two surfaces at the end of the laser. The right side output of the laser will then be given by:

$$\hat{O}_f = \hat{E}_f(L)\sqrt{1 - R^2}$$

The 1st-order rate equations (1,4) and the BC relationship (5) comprise a basic distributed model of the laser, describing both the temporal and spatial evolution of the laser operation. The presence of gain dispersion is an important feature of optical amplifiers and FP lasers determining the pulse evolution and longitudinal mode distributions. Such dispersion can be incorporated by a frequency dependent polarization term [14], [16], [22]. Although the longitudinal mode structure is a less dominant feature of grating-based lasers gain dispersion can be incorporated in the same manner.

B. SIMULATION AND INTEGRATION

Simulation of TWM models is typically done in a *stand-alone* manner where the simulation configuration is started from off or in a simple initial condition. It is then time-stepped to a final state using a discretized version of (1). However, as presented in [14] and [16] the TWM model is also very well suited for incorporation into a circuit/system-level simulator. This section will review the straightforward discretization scheme and then outline the methodology presented in [14] for incorporation of the TWM into a circuit simulator based on modified nodal analysis (MNA).

---

[1]A ˆ over a symbol indicates a complex value.

[2]It should be noted that $v_g = d\omega/dk$ is determined by the waveguide effective index and the dispersion relationship. However, the bandwidth of the envelope modulation is assumed to be sufficiently small that v_g at the carrier frequency can represent the velocity for all components and the equations in (1) will not capture dispersive effects other than that of a gross velocity modification. Other dispersive effects can be modeled by the addition of a frequency dependent polarization term or a non-zero $\hat{\kappa}$ [14].

[3]The operator * indicates complex conjugation.

1) NUMERICAL MODEL

The TWM numerical model described by (1) is formed by discretizing both space and time with $z \rightarrow z_i$ and $t \rightarrow t_j$. Several steps are taken to minimize numerical errors. The upwind formulation is used for the spatial derivatives:

$$\frac{\partial \hat{E}_f(z_i, t_j)}{\partial z} = \frac{\hat{E}_f(z_i, t_{j-1}) - \hat{E}_f(z_{i-1}, t_{j-1})}{\Delta z}$$

$$\frac{\partial \hat{E}_r(z_i, t_j)}{\partial z} = \frac{\hat{E}_r(z_{i+1}, t_{j-1}) - \hat{E}_r(z_i, t_{j-1})}{\Delta z}.$$

The time derivative is discretized as usual,

$$\frac{\partial \hat{E}_f(z_i, t_j)}{\partial t} = \frac{\hat{E}_f(z_i, t_j) - \hat{E}_f(z_i, t_{j-1})}{\Delta t},$$

but it is important that a synchronization condition given by ($\Delta z = v_g \Delta t$) is used [11]. Direct integration of the basic propagation equation motivates using an exponential ($e^{-i\hat{\beta}(z_i)\Delta z}$) rather then the 1st-order approximation ($1 - i\Delta z \hat{\beta}(z_i)$). These steps all greatly improve numerical accuracy.

Using this approach we obtain explicit time domain expressions for the unknowns in terms of the previous time-step. For example:

$$\hat{E}_f(t_j, z_i) = \hat{E}_f(t_{j-1}, z_{i-1})e^{-i\hat{\beta}(z_i)\Delta z}$$
$$+ i\Delta z \hat{\kappa}_f \hat{E}_r(t_{j-1}, z_{i+1}) + \hat{F}_f(t_{j-1}, z_i) \quad \text{(6a)}$$

$$\hat{E}_r(t_j, z_i) = \hat{E}_r(t_{j-1}, z_{i+1})e^{-i\hat{\beta}(z_i)\Delta z}$$
$$+ i\Delta z \hat{\kappa}_r \hat{E}_f(t_{j-1}, z_{i-1}) + \hat{F}_r(t_{j-1}, z_i). \quad \text{(6b)}$$

Using a similar approach for the N equation we obtain explicit time domain expressions for all the variables and the solution can simply be marched from a known state to a future one.

2) TWM-BASED DEVICES AS CIRCUIT ELEMENTS

Work has been ongoing into the development of a wide variety of approaches for optical circuit-level simulation, both academic and commercial [1], [2], [3], [4], [5], [6], [7], [8]. In particular, the work described in [23] implements a fully integrated optical/electrical simulator (*OptiSPICE*) using the MNA framework commonly used in electrical circuit simulation. The MNA method converts a system of coupled equations governing connected electrical devices into a set of nonlinear algebraic-differential equations and represents them in matrix form [24]. The method represents devices with "stamps" which relate the inputs (typically voltages) to outputs (usually currents). The system or circuit-level equations can be created by "stamping" each element into a set of 1st-order nonlinear algebraic-differential equations. These global equations are then simulated in the time domain using an implicit integration technique with Newton-Raphson (NR) iterations performed at each time-step [25].

To include optical elements in such a framework an appropriate definition of an *optical-node* for guided-wave devices is needed [23]. The basic *optical-node* is represented as two
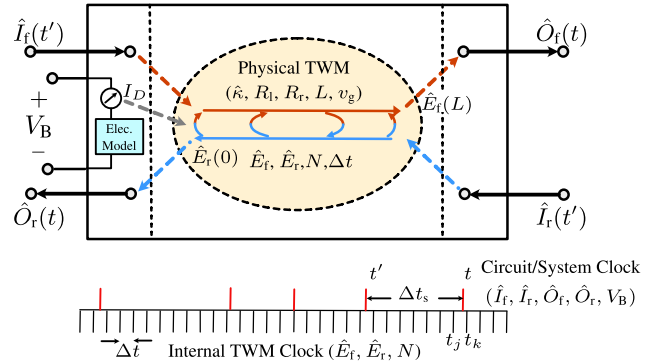
FIGURE 2. Traveling waveguide compact model: Three inputs are shown—the two complex optical inputs ($\hat{I}_f$ and $\hat{I}_r$) and an input voltage (V_B). The three outputs are the optical output fields ($\hat{O}_f$ and $\hat{O}_r$) and the device current (I_D) present between the two electrical contacts. The internal variables are the carrier density N and the forward and reverse propagating complex fields $\hat{E}_f$ and $\hat{E}_r$. The model provides an evolution from t' to $t' + \Delta t$ to allow for the calculation of the output values at t. In general, Δt_S will vary, but $\Delta t = \Delta z/v_g$ is a constant. Dashed lines imply an interpolation with respect to time is present for the connections to the internal model.

modulated waves propagating in the forward and reverse directions with the forward and reverse complex envelopes defined as $\hat{O}_f(t)$ and $\hat{O}_r(t)$ respectively. The use of a complex envelope removes the burden of modeling the quick variation of the signal at the carrier frequency. However, it also decouples the forward and reverse traveling components of the electromagnetic modes, resulting in the need to model forward and reverse traveling signals independently.

The TWM model is a flexible physical optical device model appropriate for devices varying from simple waveguide elements to lasers and is well suited for a variety of circuit-level simulation approaches. The assumptions of the TWM model: removal of the carrier and two counter propagating signals, is nicely compatible with the use of *optical-nodes* in a spice-like simulator. The task of formulating the TWM as a compact model for use in such a simulator is essentially to create a model that can be "stamped" into the global system matrix and was addressed in detail in [14]. We shall briefly summarize the approach—which is complicated by two aspects of the TWM. Firstly, the model is an explicit time stepping method, whereas the MNA formulation is implicit and involves solving a nonlinear set of equations using NR iterations. Secondly, the internal time-step (Δt) must be specified by the synchronization condition and is generally much shorter than the time-step (Δt_S) associated with the system/circuit-level simulation [26]. These two aspects of the TWM indicate that the model cannot be directly stamped into the system matrix. To solve this issue the TWM compact model is formulated as a nonlinear circuit element.

Fig. 2 illustrates the incorporation of the physical TWM model into an infrastructure where the inputs and outputs are isolated from the physical model. The three input nodes represent the forward traveling wave incident at the left facet of the device ($\hat{I}_f$), the reverse traveling wave incident at the

right facet of the device ($\hat{I}_r$) and the applied voltage (V_B). The outputs are the traveling waves leaving the device facets ($\hat{O}_f$ and $\hat{O}_r$) and the device current (I_D). All of these model inputs and outputs are determined by times specified by the system time-stop Δt_S. The relationships between the outputs and inputs are determined by the physical TWM model's evolution from a known state at t_j to the desired time t [14] and are interpolated to provide the outputs at the system time-steps.

It is very important that the compact model provides the output values at any time t without disturbing the required synchronized internal time stepping of the model [14]. The clock of the TWM element will be quantized with a time-step of Δt. The solution points demanded by the MNA engine will generally not line up with the TWM time points. Therefore as shown in Fig. 2 when new output values are required for the element the TWM model must be advanced from the last known state (t_j) to a state (t_k) just past the desired time point at t and interpolation is used to determine the values passed into and out of the internal model. Using this procedure the TWM will simulate with a very high bandwidth of $1/\Delta t$. As analytical derivatives of the outputs with respect to the inputs are not available numerical derivatives can be used in forming the Jacobian for the MNA solution [14].

3) STEADY-STATE AND OPERATING POINTS
Although typically stand-alone simulations are run from *off* circuit simulation often needs to be performed from a known OP. Obtaining such a SS initial circuit solution can involve many NR iterations. It is therefore desirable to have a quick method of obtaining an OP of the TWM compact model.

For simple waveguide elements with a prescribed detuning, gain or loss captured by $\hat{\beta}(z)$, finding a SS configuration of the TWM is straightforward as the update equations (6) can be written for the SS condition,

$$\hat{E}_f(z_i) = \hat{E}_f(z_{i-1})e^{-i\hat{\beta}(z_i)\Delta z}$$
$$\hat{E}_r(z_i) = \hat{E}_r(z_{i+1})e^{-i\hat{\beta}(z_i)\Delta z}.$$

These equations are valid for all points except for the initial point which is a known input and both $\hat{E}_f(z_i)$ and $\hat{E}_r(z_i)$ can be found by direct calculation.

For Fabry-Pérot (FP) lasers it was found in [16] that a three-step process was able to efficiently find an OP.[4] For the first step a single dominant mode is assumed and SS state equations written in terms of the magnitude of the envelope (with the phase of the mode removed). This produces this set of equations,

$$|\hat{E}_{f,k}| = |\hat{E}_{f,k-1}|e^{-i\hat{\beta}_k\Delta z} \tag{7a}$$

$$|\hat{E}_{r,k}| = |\hat{E}_{r,k+1}|e^{-i\hat{\beta}_{k+1}\Delta z} \tag{7b}$$

[4]It should be noted that a laser does not have a well defined OP. The nature of the dynamics and the presence of SPE result in a harmonic SS with stochastic variation present. However, in [16] it was shown that for a Fabry-Pérot laser a practical solution could be found that was effective and efficient.

$$S_k = \left|\hat{E}_{f,k}\right|^2 + \left|\hat{E}_{r,k}\right|^2 \tag{7c}$$

$$N_k = \left[\frac{\eta I_d}{qV_l} + g_f G_0 N_{tr} S_k\right]\left[g_f G_0 S_k + \frac{1}{\tau_n}\right]^{-1}, \tag{7d}$$

where

$$\hat{\beta}_k = \frac{1}{2}\left[\delta + \alpha_H g_k + i(g_k - \alpha_b)\right] \tag{8}$$
$$g_k = g_f G_0(N_k - N_{tr}).$$

These equations can be simply iterated and a solution found quickly. This can be done as the photon density is only dependent on the field magnitudes and allows a solution to be found regardless of dominant mode chosen. Even though the resultant single mode OP (denoted as the Fast Steady State (FSS) solution) is a good approximation when used to start the TWM it will produce a small transient. This is because the TWM is sensitive to matching N with the total photon density determined by $\hat{E}_f$ and $\hat{E}_r$ and even a close approximation may have a significant transient.

To eliminate this transient we run the exact TWM algorithm on the FSS without the stochastic forcing of the SPE producing a deterministic evolution that can be run to convergence. With no SPE present the solution will stay in the dominant mode as there is no physical mechanism to create power in the other modes. Although this step (which we will refer to as Fine Tuned Steady State (FTSS)) is significantly more computationally intensive than the FSS (typically in the order of tens of thousands of iterations) it obtains a very clean single-mode OP solution with no significant transient [16]. To form a complete OP solution, however, energy must be added into the other harmonic modes of this stationary laser solution. To add the appropriate energy to the other modes of the OP a short *pre-simulation* (PS) using the full TWM transient model including SPE can be used to naturally add harmonic content from other modes [16].

III. GRATING-BASED DEVICES
Inclusion of gratings into a TWM is well documented and involves the use of a coupling coefficient $\hat{\kappa}$ that models the scattering of the counter-propagating waves [20], [27].

A. SIMPLE GRATINGS
1) TRAVELING WAVE MODEL
The additional coupling terms present in the TWM when a grating is present can be derived from the 2st-order wave equation. Generally, the grating is modeled as a sinusoidal modulation of the permittivity,

$$\epsilon = \epsilon_0\left(1 + \Delta_\epsilon \cos(2k_B z)\right),$$

where Δ_ϵ prescribes the *depth* of the grating and $\Lambda = \pi/k_B = \lambda_B/2$ is the periodicity. The value of $\hat{\kappa}$ when the carrier frequency (ω_c) is at the Bragg frequency of $\omega_B = k_B v_g$ is found to be [20],

$$\hat{\kappa} = \frac{\Delta_\epsilon k_B}{4}. \tag{9}$$

The use of $\hat{\kappa}$ in the TWM can model both index and gain gratings [28]. For the case of index gratings power conservation requires $\hat{\kappa}_f = \hat{\kappa}_r^*$ and for the cosine grating given we have simply a single real $\hat{\kappa}$.

The direct modulation of the envelopes $\hat{E}_f$ and $\hat{E}_r$ creates frequency content off ω_c and in most of the TWM literature ω_c is set to ω_B. However, when using the TWM in a circuit configuration, it may well be needed to set ω_c at a different value. The TWM allows for two approaches to *detuning* ω_c from ω_B. We can directly use the detuning parameter (δ) present in (1) and use (9) to define the coupling coefficients which are constant along the grating. However, the modeling of coupled counter-propagating waves for this case where $\omega_c \neq \omega_B$ was addressed in [27] and it was shown an implicit offset of ω_c can also be accommodated by a coupling coefficient with a phase dependence on z described by,

$$\hat{\kappa}_{f,r} = \kappa e^{\mp j2\Delta k z}, \qquad (10)$$

where $\Delta k = k_B - k_c$. A derivation of the TWM for a cosine grating from a 2st-order wave equation showing this relationship is given in App. A.

A number of grating applications have used apodized and chirped gratings in which the depth or period is modulated along the length [29], [30], [31], [32]. Such a case can be easily accommodated by simply letting $\hat{\kappa}$ or k_B be functions z giving,

$$\hat{\kappa}'_{f,r}(z) = \kappa(z)e^{\mp j2\Delta k(z)z}.$$

A second modification to the discretized form of the simple TWM grating model of (3) is needed to address the conservation of energy. Appendix B shows the derivation of a factor f_E which addresses this issue resulting in (for a simple grating),

$$\hat{E}_f(t_j, z_i) = f_E \hat{E}_f(t_{j-1}, z_{i-1}) + i\Delta z \hat{\kappa}_f \hat{E}_r(t_{j-1}, z_{i+1}) \qquad (11a)$$

$$\hat{E}_r(t_j, z_i) = f_E \hat{E}_r(t_{j-1}, z_{i+1}) + i\Delta z \hat{\kappa}_r \hat{E}_f(t_{j-1}, z_{i-1}), \qquad (11b)$$

where $f_E = \sqrt{1 - |\Delta z \hat{\kappa}|^2}$. This factor should be added to the full discretized equations (6) when simulating more complex configurations.[5]

The assumption of a cosine grating in the derivation of $\hat{\kappa}$ is, obviously, a significant consideration and a great deal of analysis on the effect of grating shape has been undertaken [20], [33], [34]. The derivation of $\hat{\kappa}$ in App. VI invokes the use of a phase matching condition to ignore a 3st-order reflected harmonic that arises for a simple cosine. For an arbitrary grating topography represented by a Fourier series expansion, it is found that the dominant contribution to the value $\hat{\kappa}$ is due to only the 1st harmonic. As will be shown later this leads to responses that are relatively insensitive to the grating shape.

[5]The formulation of the TWM presented in [20] includes this factor, but does not present it as explicitly.

2) GROUP VELOCITY AND DISPERSION

In the TWM described by (1) the envelope propagation is characterized by the velocity v_g which for a simple waveguide is determined by the dispersion relationship $\omega(k)$ of the mode. However, in the presence of a grating it is expected that the effective v_g will need to be determined by the dispersion relationship of the periodic grating placed in the waveguide. The presence of a grating will cause a reduction in the velocity and a distortion (spreading) of pulses as they propagate. The time-domain TWM model (1) implicitly includes a 1st-order dispersion relationship. However, it is useful to compare time-domain results to frequency-domain relationships for idealized structures of infinite length. There are two appropriate ways to determine the dispersion relationship—either start with the 2st-order equation from which the TWM is derived or use the 1st-order TWM equations directly.

A rigorous derivation of the dispersion relationship will start with a 2st-order scalar wave equation with a cosine perturbation of the permittivity,

$$\frac{d^2\hat{E}}{dz^2} - \frac{1}{v_g^2}(1 - \Delta_\epsilon \cos(2k_B z))\frac{d^2\hat{E}}{dt^2} = 0, \qquad (12)$$

where k_B determines the grating period and Δ_ϵ the depth of the modulation. The wave velocity v_g in this equation would be the carrier mode velocity for a simple waveguide.

An appropriate solution for the problem is a Floquet-Bloch expansion [35],

$$\hat{E} = \sum_{n=-\infty}^{\infty} \hat{E}_n e^{j(\omega_c t - nk_B z)} e^{j\hat{K}z},$$

where $\hat{K}$ is associated with a reciprocal lattice vector of the grating. As shown in App. C the substitution of this solution into (12) produces a generalized eigenvalue matrix equation of the form,

$$\mathbf{A}(\omega, k_B, \Delta_\epsilon)\Psi = \hat{K}\mathbf{B}(k_B)\Psi.$$

The solution of this equation for a specific ω value will provide a set of $\hat{K}$ eigenvalues. If a given $\hat{K}$ eigenvalue is real the mode propagates, whereas a complex $\hat{K}$ implies an evanescent mode and the presence of a stop-band. Using this equation a dispersion relationship $\omega(\hat{K})$ can be obtained by simply solving over a range of ω values and determining $\hat{K}$. The effective velocity of signals in the grating can be determined from $v_g'(\omega) = d\omega/d\hat{K}$, where v_g' is understood as the corrected carrier velocity for a grating.

The TWM equations can also be used to derive a dispersion relationship directly [28]. We assume a time dependence of $\exp(i\delta v_g t)$ where the detuning is, $\delta = (\omega_c - \omega_B)/v_g$, and write the TWM equations in the frequency domain,

$$i\delta \hat{E}_f = -\frac{\partial \hat{E}_f}{\partial z} + i\hat{\kappa}\hat{E}_r \qquad (13a)$$

$$i\delta \hat{E}_r = +\frac{\partial \hat{E}_r}{\partial z} + i\hat{\kappa}\hat{E}_f, \qquad (13b)$$

a)

b)
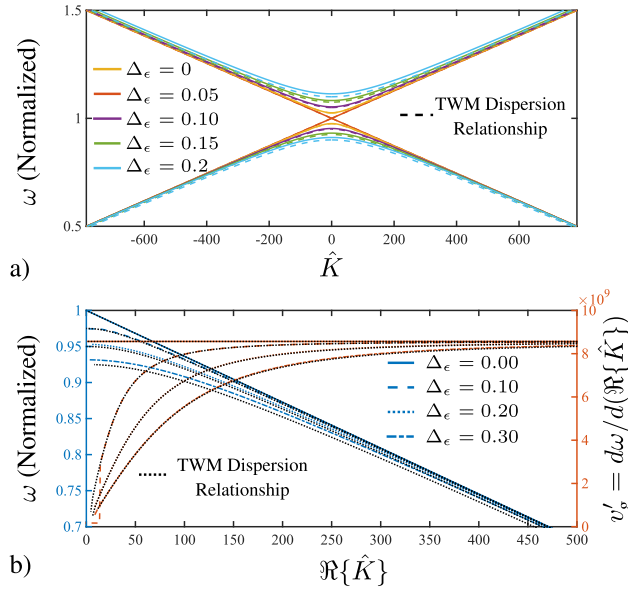
FIGURE 3. Dispersion relationship and group velocity for a cosine grating. a) $\omega(\hat{K})$ for no grating and three modulation depths. b) Lower right hand quadrant of a) showing both the dispersion relationship and the group velocity v'_g.

defining,

$$\delta = \frac{\omega_c - \omega_B}{v_g}.$$

A general solution to this set of equations, assuming no gain or loss, has the form of

$$\hat{E}_f = \hat{f}_1 e^{iKz} + \hat{f}_2 e^{-iKz}$$
$$\hat{E}_r = \hat{r}_1 e^{iKz} + \hat{r}_2 e^{-iKz}.$$

After substitution of this into (13) we find that we have non-trivial solutions (see App. D) when,

$$K = \frac{1}{v_g}\sqrt{(\omega_c - \omega_B)^2 - \kappa^2}.$$

For this simple analytical relationship we can find an effective group velocity v'_g

$$v'_g = \frac{d\omega_c}{dK} = v_g \sqrt{\frac{(\omega_c - \omega_B)^2 - \kappa^2}{(\omega_c - \omega_B)^2}}.$$

To illustrate this effect, in Fig. 3 the two dispersion relationships for a cosine grating are shown for modulations (Δ_ϵ) of 0.05, 0.10, and 0.20. The clear presence of a stop-band is evident—as expected it increases in magnitude for larger Δ_ϵ. There is a small difference between the two dispersion relationships as we approach the Bragg frequency which increases as Δ_ϵ becomes larger.

In Fig. 3b the group velocity of the grating v'_g is shown for both cases and a significant drop is predicted for $\hat{K}$ values close to zero as ω_c approaches the edge of the band-stop. Both methods give very similar predictions of the group velocity. As both the 1st and 2st-order analyses give essentially the same reduction in velocity and the TWM implicitly includes

a)

b)
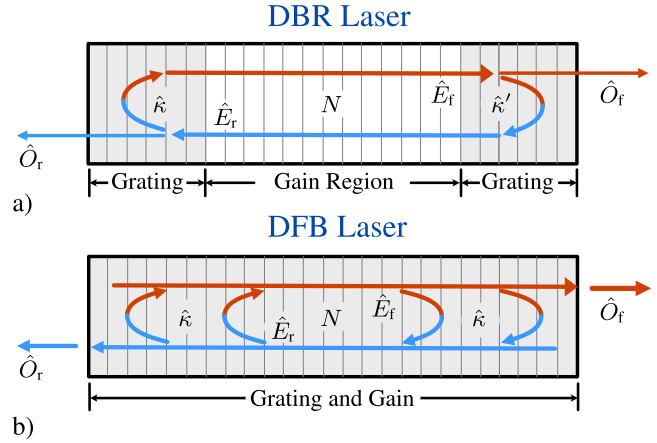
FIGURE 4. Grating-based lasers: a) DBR structure showing the central FP cavity with current injection where the FP mirrors at each end have been replaced by Bragg gratings. These gratings do not have current injection. The two gratings may not have the same reference plane and $\hat{\kappa}' = \hat{\kappa}\exp(i\alpha)$ where α is a phase shift between the two gratings. b) DFB structure showing how the FP cavity with current injection has been replaced by a Bragg grating with current injection and gain. Unlike the FP there are no mirrors at the ends. The grating itself is a distributed mirror.

the 1st-order correction, we expect the model to predict the velocity change and pulse dispersion accurately.

3) PASSIVE GRATING STRUCTURE OPERATING POINTS
For simple gratings such as described by (3) analytical solutions are available for some situations [27]. However, in general (6) can be simplified for static gratings under steady-state to,

$$\hat{E}_f(z_i) = \hat{E}_f(z_{i-1})e^{-i\hat{\beta}(z_i)\Delta z} + i\Delta z \hat{\kappa}\hat{E}_r(z_{i+1})$$
$$\hat{E}_r(z_i) = \hat{E}_r(z_{i+1})e^{-i\hat{\beta}(z_i)\Delta z} + i\Delta z \hat{\kappa}\hat{E}_f(z_{i-1}).$$

These equations are valid at all interior points and (when combined with the boundary conditions (inputs) of the grating) can be formulated as a matrix equation with the unknowns defined by $\hat{E}_f$ and $\hat{E}_r$. This equation can be easily and quickly solved to find an initial configuration of the fields.

B. GRATING-BASED LASERS
The creation of TWM models of grating-based laser structures such as the Distributed Bragg Reflector (DBR) and Distributed Feedback laser (DFB) is straightforward given an understanding of the coupling phenomena. A significant amount of literature associated with stand-alone simulation of a wide variety of effects in these laser structures has been reported [20].

Grating-based lasers are created by replacing the mirrors in a FP laser with gratings. Figure 4 shows the geometric features of the two configurations: DBR and DFB.

1) DBR TRAVELING WAVE LASER MODEL
Lasers based on DBRs are created by replacing the mirrors at one or both ends of a FP cavity with gratings (see Fig. 4a). As in a FP laser, gain is present in the central region due

to the injection of holes and electrons. The gratings act as narrow-band reflectors and provide optical feedback causing the light to pass through the gain section repeatedly. Bragg gratings strongly reflect light near the Bragg frequency, acting as an excellent mirror for this frequency while passing all others. This high frequency selectivity reduces the gain requirements on the central gain section compared to a FP laser.

Implementing a DBR configuration with the TWM simply requires a spatial variation of the current injection (see (4)) $I_D(z)$ and the coupling coefficient $\hat{\kappa}$. The central section is configured as a simple TWM waveguide section with current injection and grating $\hat{\kappa}$ equal to zero while the end sections have constant non-zero $\hat{\kappa}$ with no current injection. Even though current is not injected into the gratings the carrier equation is still implemented in them as carriers will be generated by the fields. The traditional reflectors at the ends of the FP cavity are not needed, of course, but they could be used to model reflectivity off the cavity ends if desired.

The relative positions of the reflective gratings have a significant impact on the spectral content of the output. If the two gratings are aligned (the separation is an even multiple of Λ) then constructive interference will not occur at the Bragg frequency ω_B, but instead at two frequencies within the stop-band either side of ω_B where the round-trip phase shift is 2π and so produces constructive interference[6] [20]. In such a situation either of these frequencies can be the dominant lasing mode after start up.

Such indeterminacy in the frequency of operation can be undesirable. The introduction of an additional delay of $d_\lambda = \lambda_B/4$ between the two gratings creates a situation where constructive interference occurs at ω_B and this is then the dominant mode of the laser. Modeling this delay between the two grating can be done in the TWM; either by shifting the reference of one of the gratings resulting in differing coupling coefficients for the two gratings, or by applying a phase shift at the interior ends of the two gratings.

In summary, no changes are required to the TWM equations to model a DBR laser—only specific laser configuration parameters. The DBR laser offers a number of advantages for some applications over FP lasers. However, issues of stability due to the separation of the reflective elements and the gain region motivates the use of fully distributed feedback by the extension of the grating throughout the laser creating a DFB laser.

2) DFB TRAVELING WAVE LASER MODEL

A DFB laser configuration (see Fig. 4b) is created by having both the grating and current injection (to produce gain) throughout the laser cavity. As in the DBR laser, for a DFB laser with a uniform grating, constructive interference is not supported at the Bragg frequency. As before, there are two

---

[6]Higher order modes where constructive interference occurs will be outside the stop-band and will not be strongly reflected by the grating and will *escape* leaving the laser after a single pass.

frequencies just inside the stop-band which produce constructive interference and possible lasing modes. Again, it usually being undesirable to have two possible lasing frequencies, a total $\lambda_B/4$ delay can be introduced (typically at the center of the laser) to create a single lasing mode at ω_B.

The introduction of a single $\lambda_B/4$ delay at the center of laser, however, creates a significantly non-uniform distribution of fields and carriers along the laser. This can lead to stability issues similar to those present in the DBR laser. The use of multiple delays such as $2 \times \lambda_B/8$ delays can alleviate these issues.

Implementing the DFB configuration with the TWM is therefore straightforward requiring the specification of $\hat{\kappa}$, any delays present, and the current injection for the entire section. As with the DBR no reflectors at the ends of the section are needed, but can be incorporated if desired.

3) OPERATING POINT DETERMINATION FOR DBR/DFB LASERS

As outlined in Sec. II-B3 a methodology for obtaining an OP for FP lasers has been presented in [16]. The methodology steps through a process of: 1) producing an approximate single mode solution (FSS); 2) obtaining a fine-tuned single mode solution (FTSS); and 3) adding harmonic content from other modes using a short pre-simulation (PS). If the TWM model of DBR/DFB lasers is to be used in a circuit simulation context the same capability to predict an OP must be developed.

Essentially, the same approach can be used for DBR and DFB lasers. If the laser is configured with a uniform grating there are two possible dominant modes—either above or below ω_B and either can be chosen to be the constructed OP. If the laser is configured using a total $\lambda_B/4$ delay the single dominant mode is at ω_B. In a similar manner to the FP laser the FSS solution can be determined and then fine-tuned with the FTSS. However, the procedure for the grating-based lasers is somewhat more complicated.

For a DBR laser the form of the central cavity field magnitude and distribution of N is the same as for FP and in the gratings the fields simply decay as there is no gain. The gratings can be characterized by an effective reflection, which can be be determined prior to finding the FSS, and the effect of N in the gratings assumed to be negligible. Then for the interior resonator we use the same procedure given in [16] for the FP and through iteration of (7) we determine the magnitude distribution which satisfies the carrier equation self-consistently creating a single mode FSS solution. Once obtained the phase modulation due to the choice of the dominant mode can be introduced and the decaying fields in the gratings added into the solution.

The DFB has only one single uniform section but produces a more complex field form. The presence of coupling requires that (7a) and (7b) need to be replaced by,

$$\hat{E}_{f,k} = \hat{E}_{f,k-1}e^{-i(\Delta\omega\Delta t + \hat{\beta}_k\Delta z)} + i\hat{\kappa}_f\hat{E}_{r,k} \quad (14a)$$

$$\hat{E}_{r,k} = \hat{E}_{r,k+1}e^{i(\Delta\omega\Delta t - \hat{\beta}_{k+1}\Delta z)} + i\hat{\kappa}_r\hat{E}_{f,k}, \quad (14b)$$
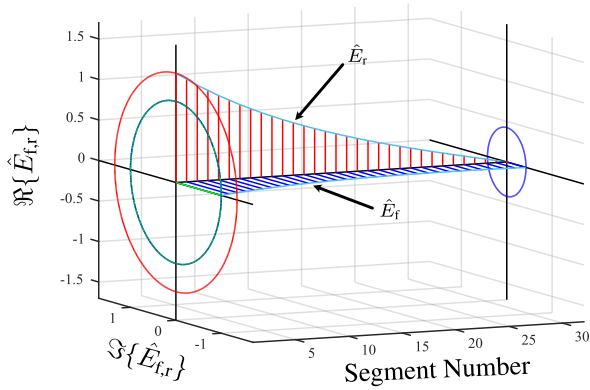
FIGURE 5. 3D plot of simple propagation through a grating segment. Input is constant field from the left. Plot shows SS complex fields: forward $\hat{E}_f$ (blue) and reverse $\hat{E}_r$ (red). The reflected fields are rotated exactly $\pi/2$ from each other. The normalized field components (real and imaginary) are plotted along the waveguide. The position of the field along the waveguide is denoted by the segment number of the TWM model.

where $\Delta\omega$ is the frequency shift from ω_B for the mode of interest. Unlike (7a) and (7b) these equations are coupled, can not be directly calculated, and will need to be iterated to find a solution. Therefore, the solution of the FSS for the DFB involves two nested iterations whereby the outer loop solves for N using (7d) having obtained $\hat{E}_f$ and $\hat{E}_r$ from iterating (14). Although for both grating-based lasers the formation of the initial FSS is more complicated than for the FP the iteration to self-consistent solution is still efficient, taking approximately 100 iterations – with the interior loop for solving (14) needing only 10 iterations for a DFB simulation.

The FTSS code is identical to the FP TWM code. It was found that due to the narrow band operation of the two grating-based lasers we do not require the PS step of the TWM OP which added in the non-dominant modes.

IV. GRATING RESULTS AND EXAMPLES
In this section we will first provide an example of the TWM with the two counter-propagating envelopes present in a grating, providing for an intuitive grasp of the model. We then investigate pulse propagation using the TWM making a detailed comparison to an FDTD simulation using a Yee-cell implementation, confirming the accuracy of the model for the questions of interest. Finally, we will illustrate the use of the TWM model for a passive application, the generation of optical codes, using this to explore system-level impacts of the TWM circuit implementation.

A. GRATING PROPAGATION
1) FIELD CONFIGURATION
An intuitive understanding of the TWM propagation through Bragg gratings can be grasped using a simple example where there is a constant input field incident from one side. Fig. 5 presents the complex field amplitudes along a grating segment with an input field incident from the left with a fixed

unit amplitude and $\hat{E}_f(t, 0) = 1$.[7] The carrier frequency is at the Bragg frequency and the coupling coefficient $\hat{\kappa}$ is real and constant. The forward field (blue) is moving to the right; the generated counter-propagating reverse field (red) is moving to the left. We see both the forward and reverse traveling fields do not rotate in time or space, but the two complex envelopes are rotated $\pi/2$ with respect to each other, as expected from the presence of the "$+i\hat{\kappa}\hat{E}_{f,r}$" terms in the TWM equations (1).

The decay in magnitude of $\hat{E}_f$ is due to the coupling of the counter-propagating field. For example, the coupling term for $\hat{E}_f$ produces a small positive imaginary contribution to $\hat{E}_r$. This imaginary contribution to $\hat{E}_r$ is in turn coupled into $\hat{E}_f$ as a negative real contribution reducing the total $\hat{E}_f$ field. As the field propagates there is a reduction at each step producing a decay in the field. In the reverse direction we have no incident field from the right and $\hat{E}_r(L) = 0$. At each step the coupling from $\hat{E}_f$ will produce a small increase in the imaginary part of $\hat{E}_r$ as it propagates to the left. This gives the basic dynamics of the grating feedback in the coupled fields.
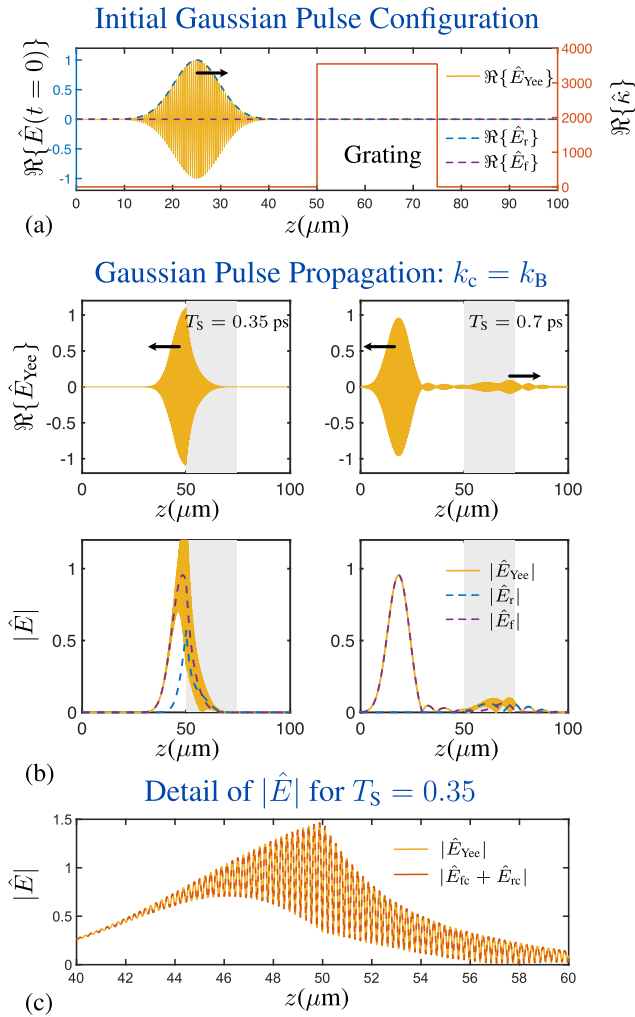
2) PULSE PROPAGATION
In order to validate the TWM grating models we implemented Maxwell's equations with a 4st-order Yee-cell implementation in 1D [36]. We use this to compare the TWM output with the predicted output from the Yee-cell simulation. Fig. 6 shows the propagation of a modulated[8] Gaussian pulse with a grating placed midway through the cavity. The excitation frequency of the pulse equals the Bragg frequency of the grating ($\omega_c = \omega_B$) and we expect the pulse to primarily be reflected. The initial pulse at $T_S = 0$ is shown in Fig. 6a and is traveling to the right. Also shown is $\hat{\kappa}$ which defines the presence of the grating.

Fig. 6b shows the pulse at two different simulation times. At $T_S = 0.35$ ps (left) the pulse peak has just reflected off the grating and at $T_S = 0.7$ ps the pulse has moved away from the grating still traveling left. As the grating is finite and short it acts as narrow band reflector with an effective reflectance. The presence of bandwidth off ω_B due to the shape of the pulse will produce a small amount of transmission. Both the reflected and transmitted pulses undergo dispersion due to the distributed nature of the "reflector".

The plots in Fig. 6b allow for a comparison of the Maxwell Yee-cell 1D FDTD simulation with the TWM. The top row of Fig. 6b shows the real fields of the Yee-cell simulation. To compare with the TWM we take the envelope of the complex Yee field and compare with the forward and reverse field amplitudes. In the bottom row we can see that when the pulse is outside the grating they match very well. When partially inside the grating, the interference pattern generated by the counter-propagating waves implicitly present in the Yee field produces an interference pattern which is difficult to

---

[7]For this section all field values are given with respect to a normalized excitation.

[8]The modulation is a complex exponential of the form $\exp(i(\omega_c t - k_c z))$.

FIGURE 6. Propagation of Gaussian pulse into grating with excitation at Bragg frequency. a) Initial configuration of a pulse showing both a Yee-cell and TWM simulation. b) Propagation of a modulated Gaussian pulse with a grating placed from $z = 50$ μm to $z = 75$ μm for two different simulation times T_S. The pulse is reflected by the grating when the excitation frequency matches the grating ($\omega_c = \omega_B$). The top row is 1D Yee-cell FDTD simulation and bottom row shows a comparison of the magnitude of the two traveling wave fields $\hat{E}_f$ and $\hat{E}_r$ to the Yee-cell result. c) Detail of the interference pattern present in the grating ($T_S = 0.35$ ps) when both the forward and reverse waves are present. Shown is the magnitude of the Yee-cell field and the summed TWM fields with the carrier included.

compare to the envelopes modeled by the TWM. We can note, however, that the average magnitude of the Yee field matches the corresponding field (dependent on direction of travel) of the TWM. We can show that the fields match exactly by introducing the carrier into the the TWM fields according to;

$$\hat{E}_{fc} = \hat{E}_f e^{i(\omega_c t - k_c z)} \quad (15a)$$

$$\hat{E}_{rc} = \hat{E}_r e^{i(\omega_c t + k_c z)}. \quad (15b)$$

In Fig. 6c we have combined the TWM fields with the carrier at $T_S = 0.35$ ps and presented the fields in detail inside the grating. We see that even for the complex interference
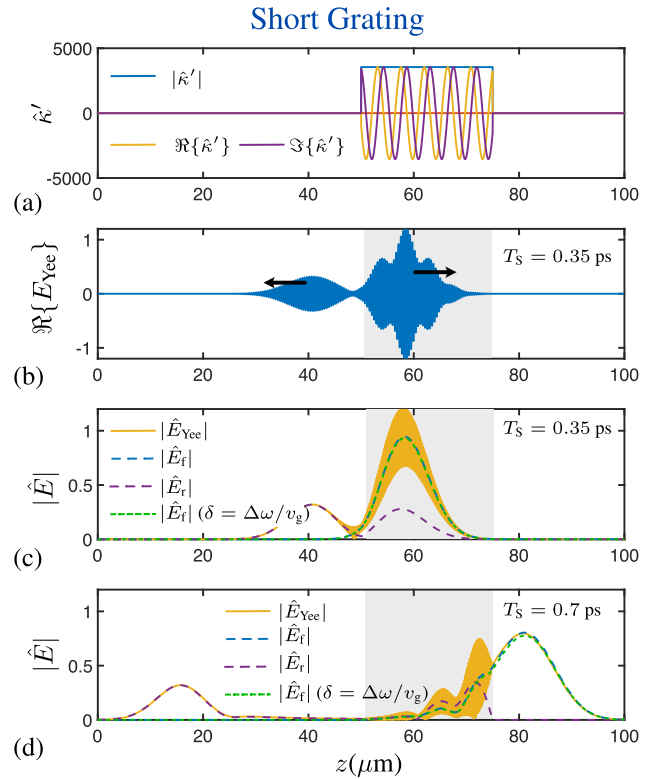
FIGURE 7. Propagation of Gaussian pulse in grating when the excitation frequency is offset from the grating frequency ($\omega_c = 1.05 \omega_B$). The basic configuration is the same as Fig. 6. a) Complex coupling parameter $\hat{\kappa}'$. b) Yee-cell simulation for $T_S = 0.35$ ps. Yee-cell and TWM simulation comparison for both types of TWM detuning: c) For $T_S = 0.35$ ps, d) for $T_S = 0.7$ ps.

pattern due to the reflection, the two models are in excellent agreement.

We now turn to the more general case where the excitation frequency of the Gaussian pulse does not equal the Bragg frequency of the grating ($\omega_c \neq \omega_B$) and partial reflection is expected. As remarked above there are two approaches to *detuning* the excitation from ω_B by $\Delta\omega$: Firstly, the introduction of a complex non-constant coupling coefficient $\hat{\kappa}'$, see (10), can be used to implicitly move the carrier; or, alternatively, the parameter δ found in (2) can be used detune the carrier with $\hat{\kappa}$ kept as constant.

The effect of detuning the transmitted frequency (ω_c) from the grating Bragg frequency (ω_B) is to decrease the coupling and lower reflection. In Fig. 7 this case (the short grating and pulse used in Fig. 6) is presented for both methods of detuning. The detuning used was such that $\omega_c = 1.05\omega_B$ and the complex modulation of $\hat{\kappa}'$ can be seen in the top panel.

The middle two plots (Fig. 7b and c) show simulations at $T_S = 0.35$ ps when the pulse has split into two—a smaller reflected pulse and a larger pulse in the grating. A comparison with Fig. 6 shows a much larger degree of transmission. Fig. 7b shows the Yee-cell real field which exhibits a complex shape due to the beating between the forward and reverse traveling components. To compare with the TWM, in Fig. 7c

the absolute fields for the Yee-cell and TWM simulations are presented and we see a very good match. The bottom plot, Fig. 7d, is at $T_S = 0.7$ ps, after the pulse has passed through the grating, and again the Yee-cell magnitude matches the TWM very well. In addition to presenting the TWM model using a complex coupling coefficient with an implicit carrier $\omega_c = \omega_B + \Delta\omega$, the plots also include a simulation where a constant coupling coefficient $\hat{\kappa}$ was used and a detuning of $\delta = \Delta\omega/v_g$. It can be seen that the same match is obtained for both methods of detuning.

In Sec. III-A1 it was noted that for propagation in a grating the simple TWM equations needed a correction factor f_E to conserve energy (see (11) and App. B). To investigate this effect on the TWM we introduce a much longer grating (400 μm), and use a complex $\hat{\kappa}'$ to detune the carrier. In Fig. 8 the results are plotted with and without the factor present. Fig. 8a, again shows $\hat{\kappa}'$ for the grating. Fig. 8b shows the simulation at $T_S = 0.6$ ps, when the pulse has split into two pulses going in opposite directions. For this short interaction time the correction factor is not impactful and both curves match the Yee-cell magnitude. Fig. 8c shows the simulation at $T_S = 5.2$ ps, after the pulse has passed through the long grating. It can be clearly seen that with the factor f_E present the match to the Yee-cell result is good, conversely if the factor is omitted ($f_E = 1$), energy is not conserved and we see an incorrect result.

3) GRATING SHAPE

The TWM characterizes the effect of the grating with two simple coupling parameters $\hat{\kappa}_f$ and $\hat{\kappa}_r$. Section III-A1 and App. VI present an expression for these parameters assuming a cosine grating with a permittivity perturbation Δ_ϵ. However, as noted in Sec. III-A1, due to phase matching it is expected that the effect of the grating will be characterized by the strength of the first harmonic. Fig. 9 illustrates this by comparing the TWM with the Yee-cell model for several shapes of permittivity. We start with a pure 1st-harmonic cosine variation and then add in a number of harmonics, n_h, of the Fourier Series expansion of a rectangular grating. A key point in presenting the results is that the fundamental harmonic of the Fourier Series in each grating has the same weighting. In Fig. 9a we see the four gratings with a transition from the pure cosine (top) to reasonable approximation of a square wave using 11 harmonics. In Fig. 9b we see, the perhaps counter-intuitive result, that not only do the TWM forward and reverse fields match the Yee-cell field magnitude, but the fields for all values of n_h also are essentially identical. This confirms that it is not the grating shape that is important but the magnitude of the fundamental period of the grating—a result also remarked upon in [34].[9]

[9]It should be noted that this 1D characterization of the grating is limited and more sophisticated models have been developed incorporating both longitudinal and cross-sectional grating and field configurations [27], [33], [34]. These models would allow for a more accurate determination of $\hat{\kappa}$ for use in the TWM.
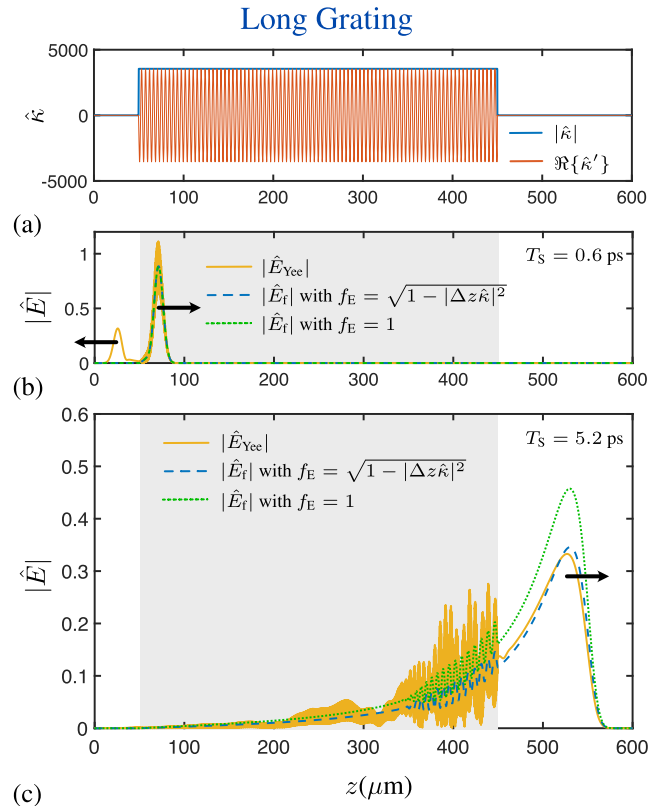

FIGURE 8. Propagation of Gaussian pulse in a long grating when the excitation frequency is offset from the grating frequency ($\omega_c = 1.05\ \omega_B$). a) Coupling coefficient and grating configuration. Propagation of Gaussian pulse for two times b) $T_S = 0.6$ ps and c) $T_S = 5.2$ ps. The initial pulse configuration was as in Fig. 6 with a grating of 400 μm. Two simulations are presented with and without the energy conservation factor f_E used.

4) GROUP VELOCITY AND DISPERSION

As discussed in Sec. III-A2 the presence of a grating will change the effective group velocity (v'_g) of a waveguide. Two derivations of the dispersion relationship are presented based on the 2st-order wave equation and the 1st-order TWM wave equations. The TWM model implicitly includes the 1st-order dispersion relationship. As presented in Sec. III-A2 they predict almost identical dispersion relationships. In order to validate the relationships we compare both of them to Yee-cell simulations through a long grating for various grating depths, varying the carrier frequency (ω_c) with a grating prescribed by ω_B. For the TWM simulations a complex $\hat{\kappa}'(z)$ was used to detune the carrier. In Fig. 10a we see the expected variation in v'_g as we approach the stop band where the wave becomes evanescent with an effective speed of zero. For the case with no grating ($\Delta_\epsilon = 0$), v'_g is equal to the nominal group velocity v_g for all three. Overall the 2st and 1st-order calculations are extremely close to each other and agree well with the Yee-cell measurement. Note that the simple speed calculation used for the Yee-cell simulation will not be as accurate as we approach the stop band frequency and the pulse slows down and becomes evanescent.

Permittivity Variation

Gaussian Pulse Propagation
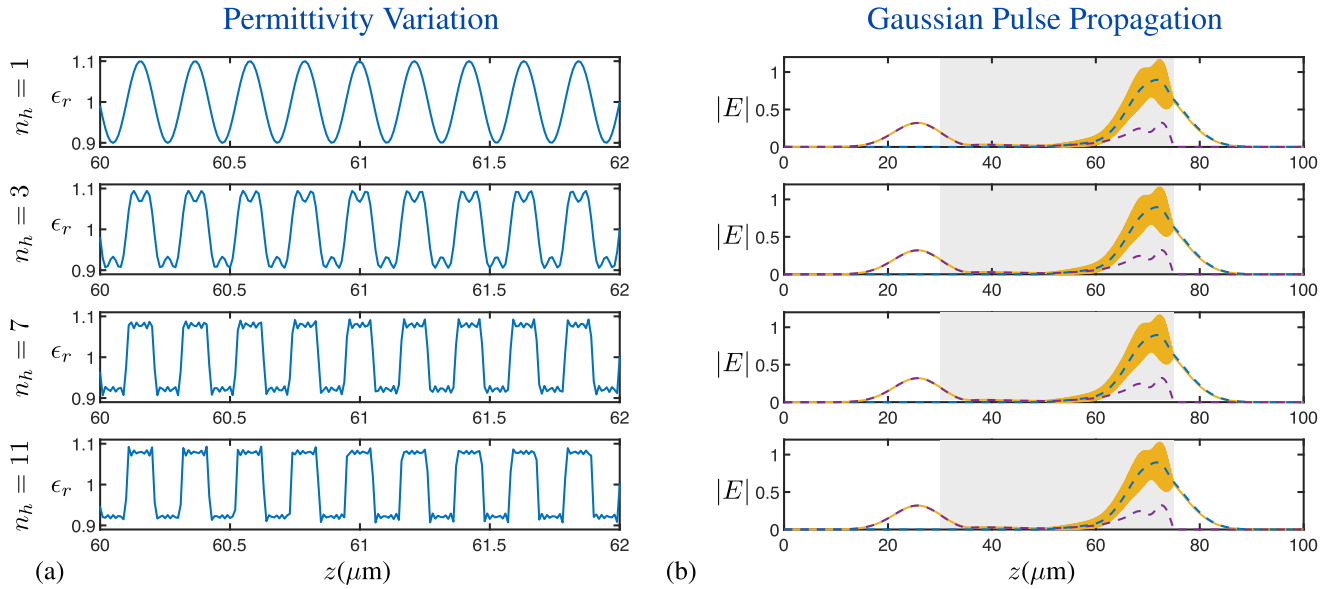
FIGURE 9. Gaussian propagation through different grating topologies. The excitation frequency is offset from the grating frequency ($\omega_c = 1.05\,\omega_B$). Simulation configuration is the same as in Fig. 6. Shown in each row is a detail of the permittivity as a function of z and a comparison between the Yee-cell and TWM simulations for $T_S = 0.6$ ps. The permittivity is varied by adding a number of harmonics n_h in a Fourier series expansion of a rectangular grating. For all gratings the fundamental harmonic has the same weighting.

Group Velocity

Gaussian Pulse Propagation
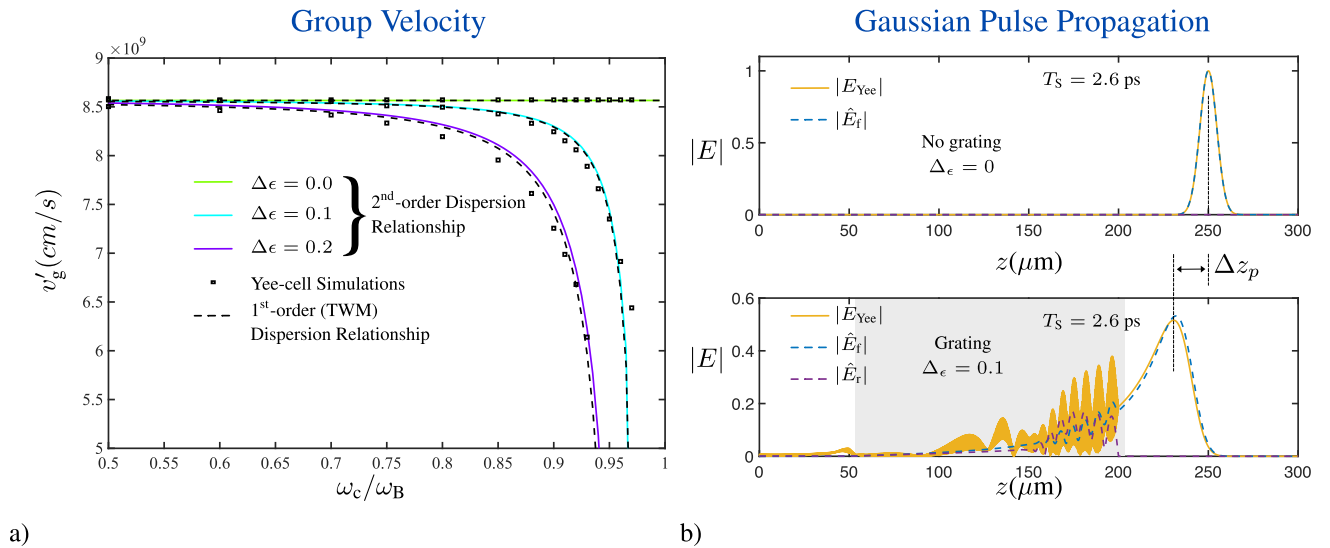
FIGURE 10. Group Velocity: a) Comparison of $v_g'(\omega)$ between analytical derivation and Yee-cell simulation. b) Gaussian propagation through a long grating showing v_g' reduction due to the dispersion relationship. The bottom plot (with grating) shows that the pulse does not travel as far in the simulation time $T_S = 2.6$ ps.

Fig. 10b shows two of the simulations for $\omega_c/\omega_B = 0.95$ used to generate the data in Fig. 10a—one with no grating ($\Delta_\epsilon = 0$) (top) and another with $\Delta_\epsilon = 0.1$ (bottom). As expected, with no grating the TWM agrees with the Yee-cell and the pulse travels at the velocity of the carrier. In the bottom plot, with $\Delta_\epsilon = 0.1$, the pulse is slowed and travels a distance shorter by Δz_p in the prescribed time. The pulse dispersion (change of shape) and the velocity reduction present in the Yee-cell simulation is well predicted by the TWM. Using the 2st-order dispersion relationship we find that Δz_p is 19.4 μm and this agrees well with the observed

value of 19.1 μm. We can conclude that the 1st-order dispersion relationship implicit in the TWM captures the velocity reduction and shape changes effectively.

B. CIRCUIT IMPLEMENTATION: OPTICAL CODE GENERATION

As an example of the use of a passive grating structure in an optical circuit we will use an implementation of a picosecond optical code generator simulated in *OptiSPICE* [6] incorporating a TWM model. Techniques for generating codes formed from short optical pulses have been developed

Optical Code Generation Circuit

a)

Grating Configuration

Pulse Propagation

b)

c)

Pulse Generation

d)
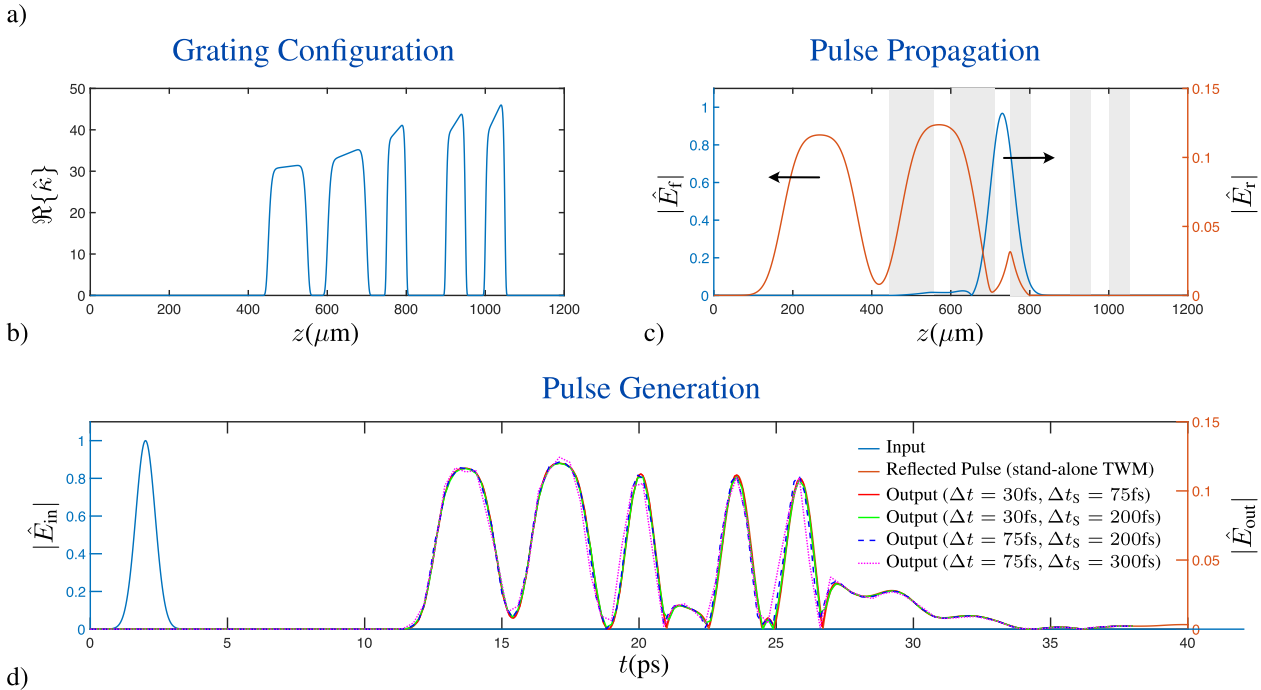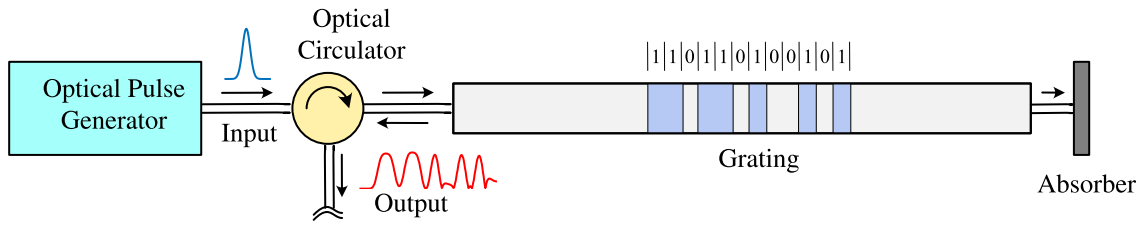
FIGURE 11. Grating Example: Optical Code Generation. a) Circuit schematic. b) Coupling coefficient $\hat{\kappa}$ plotted along the grating. c) Field configurations as the incident pulse propagates through the grating. d) Circuit output for a variety of time-step configurations. Also shown is a stand-alone TWM simulation of the grating.

with varying levels of sophistication [37], and implementations have included fiber Bragg gratings [38] and array waveguide devices [39]. However, an attractive alternative is integrated waveguide devices [32]. The use of an integrated device allows for very fine control of the grating topography enabling chirping or apodization of the grating. Such engineering of the grating manifests as spatially varying coupling coefficients in the TWM model.

As described in [32], an integrated waveguide-based grating can be configured to produce an optical code consisting of a set of picosecond length pulses. A simple circuit implementing a code generation application is presented in Fig. 11. The circuit consists of an optical pulse generator, an optical circulator to redirect the code generated (in reflection) from the grating, a configured grating, and an absorber. The basic operation of code generation is to have a pulse incident on the grating with $\omega_c = \omega_B$, where the grating is spatially configured to reflect back a sequence of pulses as the pulse traverses it, creating the code.

The grating can be configured quite simply if 2st-order FP reflections are negligible—requiring that the grating segments generating each pulse are only extracting a small amount of the incident power. In this case the binary code to be generated can literally be simple *written* in space along the grating with alternating sections of uniform waveguide and grating.[10] For the TWM this is modeled as a spatially varying $\hat{\kappa}$, with a value of zero being present for the waveguide sections. One consequence of the nature of the application is that later *bits* in the code are generated by a broader forward traveling pulse of diminishing magnitude.

In Fig. 11b and c we can see the internal aspects of the TWM model. The first figure shows the configuration of the grating in which a sequence of grating regions are placed. All grating regions have the same pitch with $\omega_B = \omega_c$. However, the grating is apodized such that the value of the coupling coefficient is engineered to produce bits of similar magnitude

---

[10]More sophisticated methods can be used to engineer the grating taking into account the FP reflections, but this simply results in a different grating configuration and no conceptional difference.
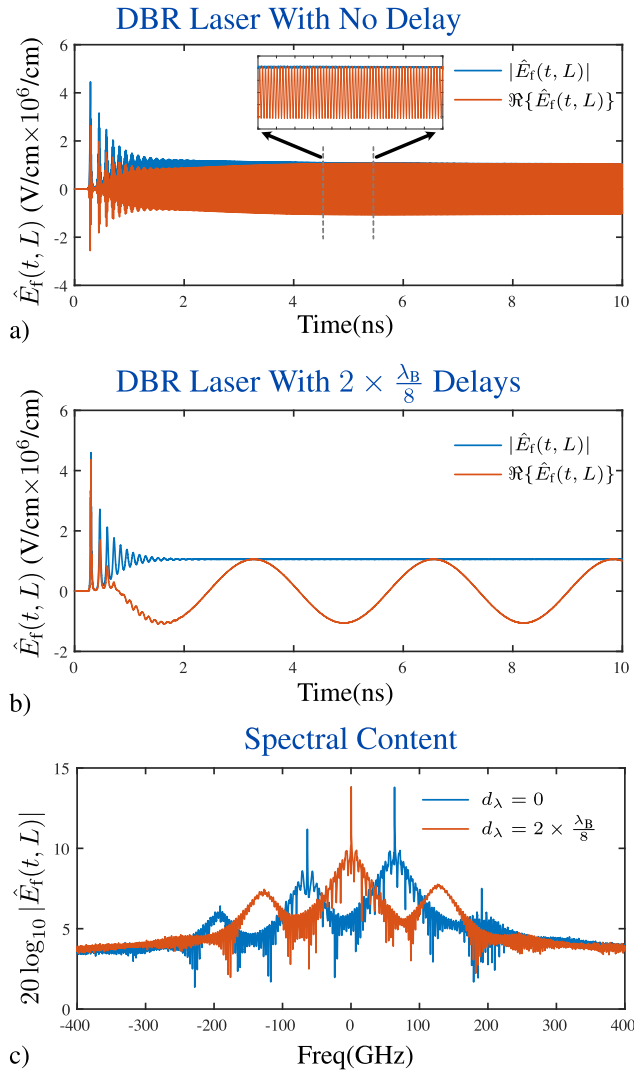
FIGURE 12. DBR Laser transients. Output field as a function of time: a) Laser with synchronous gratings (no delay), b) Laser with a total of $\lambda_B/4$ delay present. c) Spectral content at harmonic SS. Obtained using an FFT of the field from the last nanosecond.

and width. The excitation pulse is a Gaussian pulse with a width of 2 ps and Fig. 11c shows a depiction of the field configuration in the TWM at the point where the incident pulse is propagating through the grating device. You can see the reflected code being formed as the incident pulse travels along the grating.

The operation of the TWM circuit element at the system level is presented in Fig. 11d which plots the incident and reflected pulses as a function of time. The optical code of 110110100101 can be clearly seen in the reflected signal and the bits are of roughly equal magnitude. The primary system-level concern is the interaction between the internal time-step Δt of the TWM and the external system time-step Δt_S. The system-level time-step will be defined by the bandwidth of excitations within the circuit. The TWM time-step will need to be generally at most half of this value, but may well be shorter as it is constrained by the spatial

configuration of the device (which determines the number of elements N_z in the TWM) and the synchronization condition ($\Delta z = v_g \Delta t$). Shown in the figure are a number of simulations for varying time-steps. To resolve the input pulse adequately a system step-size less then $\Delta t_S = 300$ fs was needed. It could be expected that for a passive device such as this, the external bandwidth would dictate the response of the device as no higher frequency components can be internally generated. Indeed, it was found that as long as the system time-step adequately discretizes the incident pulse and the internal time-step was smaller than this value, the circuit simulation reproduced the stand-alone TWM simulation with no bandwidth limitations (except of course those imposed by the internal time-step).
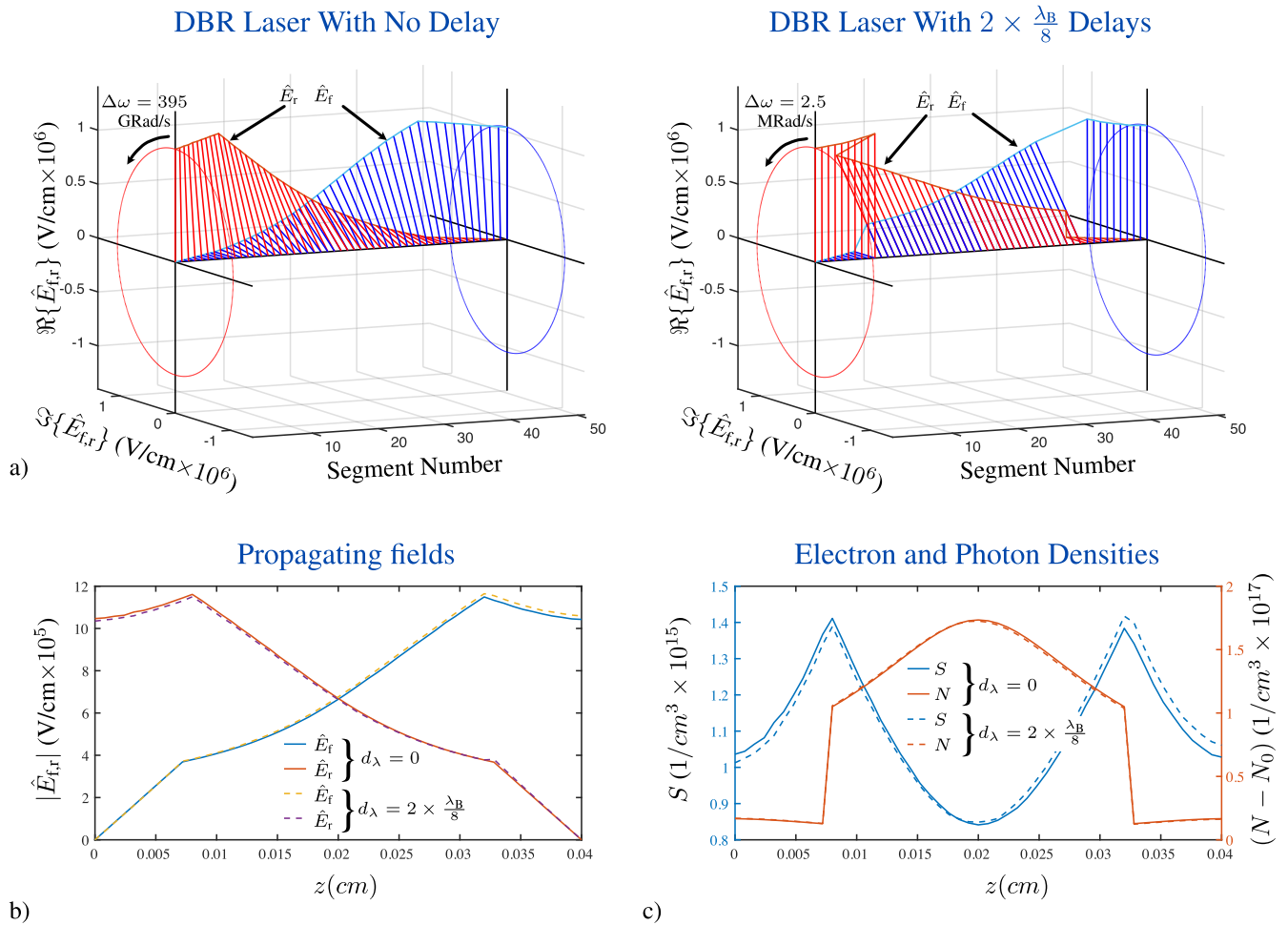
V. LASERS RESULTS
In this section we will deal with the TWM simulation of the two grating-based lasers of interest: DBR lasers, configured with two distributed reflectors and an internal gain region; and DFB lasers with a full grating throughout the laser cavity. The first part of this section will demonstrate the TWM ability to capture the essential behaviour of the two lasers using the simulation of full transients for a variety of configurations. These simulations will be used to illuminate a number of aspects that influence the use of the TWM for laser simulation in a circuit context. The second part of this section will deal explicitly with circuit aspects of the laser simulation. Firstly, it will show the effectiveness of the operating point determination for the two laser configurations. Then, the simulation of full transients will be used to demonstrate the use of detuning to allow for an increase in the system time-step. Finally, an example of a directly modulated DFB laser will be used to illustrate the interaction of the system time-step and simulation stability in the presence of a back reflection.

A. FULL TRANSIENT SIMULATIONS
1) DBR LASER
The DBR laser fundamentally operates in a manner very similar to the FP laser with a central gain cavity and mirrors at each end. The two mirrors are, however, Bragg gratings which create a narrow-band distributed reflector. As in the FP laser, current is injected into the central cavity creating a gain region. Lasing is initiated by spontaneous emission and a lasing mode will be created. Light at the Bragg frequency will be most strongly reflected by the gratings, but the phase of the reflected light at this frequency does not produce constructive interference so this frequency will not lase. However, two frequencies ($\omega_c = \omega_B \pm \Delta\omega$) at the edges of the grating stop band will be reflected with a phase appropriate for lasing and either of these modes can become the dominant lasing mode. The frequency offset $\Delta\omega$ is determined by the length of the gain cavity and the grating configuration. Frequencies outside of the stop band are not reflected strongly and do not produce lasing.

Complex Fields

DBR Laser With No Delay

DBR Laser With $2 \times \frac{\lambda_B}{8}$ Delays

a)

Propagating fields

b)

Electron and Photon Densities

c)

FIGURE 13. DBR internal configuration after a full transient: a) Complex field propagation for two laser configurations. Note that these fields are rotating as well as traveling. The fields for the configuration with no delay (left) rotate quickly in the CW direction, giving the high frequency envelope component. The fields with a total of $\lambda_B/4$ delay (right) rotate very slowly resulting in no high frequency components. b) Field magnitudes. c) Electron and photon densities. The introduction of the $\lambda/8$ delays does not change the field amplitudes or internal densities significantly.

The presence of two possible lasing modes at $\omega_B \pm \Delta\omega$ is usually undesirable, so, by placing a $\lambda_B/4$ delay between the two reflectors, such that they are no longer spatially synchronized, ω_B becomes the dominant lasing frequency. In the TWM model this delay can be implemented either with a change in the reference for $\hat{\kappa}$ in one of the gratings (resulting in a different $\hat{\kappa}$ for each grating) or by implementing a phase delay of $\lambda_B/8$ in the TWM model on each interior grating edge.

Full transient simulations are shown for both laser configurations in Fig. 12. The top figure shows a full transient and detail for a default DBR laser with synchronized gratings (no delay), $\hat{\kappa} = -50$ in both reflectors and the implicit carrier is at ω_B. The laser undergoes a transient and produces a harmonic SS and it is clear that the final state is off the Bragg frequency due to the fast oscillation of the envelope (see the detail). This frequency shift is also evident in Fig. 12c which presents the spectral content of the harmonic SS. The spectrum was

obtained using an Fast Fourier Transform (FFT) of the field from the last nanosecond. Both lasing modes are clearly present with the dominant mode at $\Delta\omega = 63$ GHz. The presence of this high frequency modulation of the envelope has important implications for using the TWM as a compact circuit model, as it will set a limit on the size of the system time-step.

In Fig. 12b we see the effect of the introduction of a total delay of $\lambda_B/4$ between the two reflectors. The frequency of oscillation is now very close to that of the Bragg frequency and the modulation is no longer present. In the plot of the spectral content we clearly see that there is now only a single lasing mode present at the Bragg frequency.

The interior configuration of the DBR laser at SS can be seen in Fig. 13. In Fig. 13a the complex field distribution of $\hat{E}_f$ and $\hat{E}_r$ are shown for the two cases of no delay and with two $\lambda_B/8$ delays. For the first case as the fields propagate through the cavity it can be seen that a spatial twist in the complex

envelopes is created, representing the shift in frequency of $\Delta\omega$. This image is a snapshot in time and the envelopes are both rotating in time at frequency of $\Delta\omega$. In contrast, when the total delay of $\lambda_B/4$ is introduced into the cavity it is manifests as two phase jumps in the fields and a very small envelope twist—consistent with ω_c being very close to ω_B and a slow rotation of the envelopes. Also presented in this figure are plots of the magnitude of the two counter-propagating fields and the carrier and photon densities along the laser. In the first the exponential nature of the fields is clearly seen—with growth in the interior gain region and decay in the gratings. The carrier and photon densities in the interior region are similar to that of a FP laser. It can be seen that the presence of a delay element in the device has little impact on these quantities, although, of course, it has a significant impact on the lasing frequency as we have seen.

2) DFB LASER

Although the DFB laser has a grating distributed throughout the laser and no distinct resonant cavity, its operation is similar to the DBR. The Bragg grating creates a narrow-band distributed reflector while current injection creates gain throughout the laser. Lasing is, as with the DBR, initiated by spontaneous emission and a lasing mode will be created for light that undergoes constructive interference when reflected by the grating. Light at the Bragg frequency, however, does not satisify this phase condition and will not lase. But as before, two frequencies ($\omega_c = \omega_B \pm \Delta\omega$) at the edges of the grating stop band will be reflected with a phase appropriate for lasing and either of these modes can become the dominant lasing mode.[11] Once again, frequencies outside of the stop band are not reflected strongly and do not produce lasing, limiting the longitudinal modes present. As with the DBR, to restrict the operation of the device to a single mode at the Bragg frequency one can introduce a total $\lambda_B/4$ delay. However, the introduction of delay elements (essentially a discontinuity in the grating periodicity) into the the uniform grating has a significant effect on the internal field, carrier and photon distributions.

A simulation of a DFB laser is shown in Fig. 14. Fig. 14a shows the transient where the laser is configured with a delay element of $\lambda_B/4$ present at the center of the grating. This has shifted the lasing frequency to ω_B and no high frequency modulation of the output envelop is present. After a few nanoseconds the laser has transitioned to harmonic SS at a very slight offset from the Bragg frequency. This can also be seen in Fig. 14b where the spectral content obtained from the last nanosecond of this simulation is presented. Also shown in this figure are three simulations of a uniform grating laser (no delay elements) for three different lengths. One obvious feature of these three simulations is that the laser can randomly (as determined by the nature of the SPE) start

up in either of the two modes available at $\omega_B \pm \Delta\omega$. Also evident is the length dependence of the lasing frequency (see footnote 11).

In the last two plots of this figure the field magnitudes (Fig. 14c) and carrier and photon densities (Fig. 14d) are plotted along the length of laser. The introduction of a single delay element of $\lambda_B/4$ at the center of the device produces a dramatic change in the fields and distributions. In particular the carrier distribution N becomes significantly non-uniform which can produce instabilities due to hole-burning and non-uniform heating. A solution to this is to introduce multiple delays of smaller magnitude and also presented in this figure is a device configured with $2 \times \lambda_B/8$ delays equally spaced along the device. Such a device has a lasing frequency of ω_B and relatively uniform carrier and photon distributions.

Having illustrated the TWM capabilities of modeling a wide variety of phenomena present in grating-based lasers we will turn to the issues present when using the model as a circuit simulator element.

B. CIRCUIT INTEGRATION

In this section we will first demonstrate the ability to generate an operating point OP (harmonic SS) for both DBR and DFB lasers using the procedures given in III-B3. We will then illustrate some of the circuit implementation issues that arise from using the TWM as a circuit simulation element. The first example will be for a simple transient from off with a comparison between the circuit simulation to the stand-alone TWM simulation. The final example will deal with direct modulation of a DFB laser to produce an output bit stream.
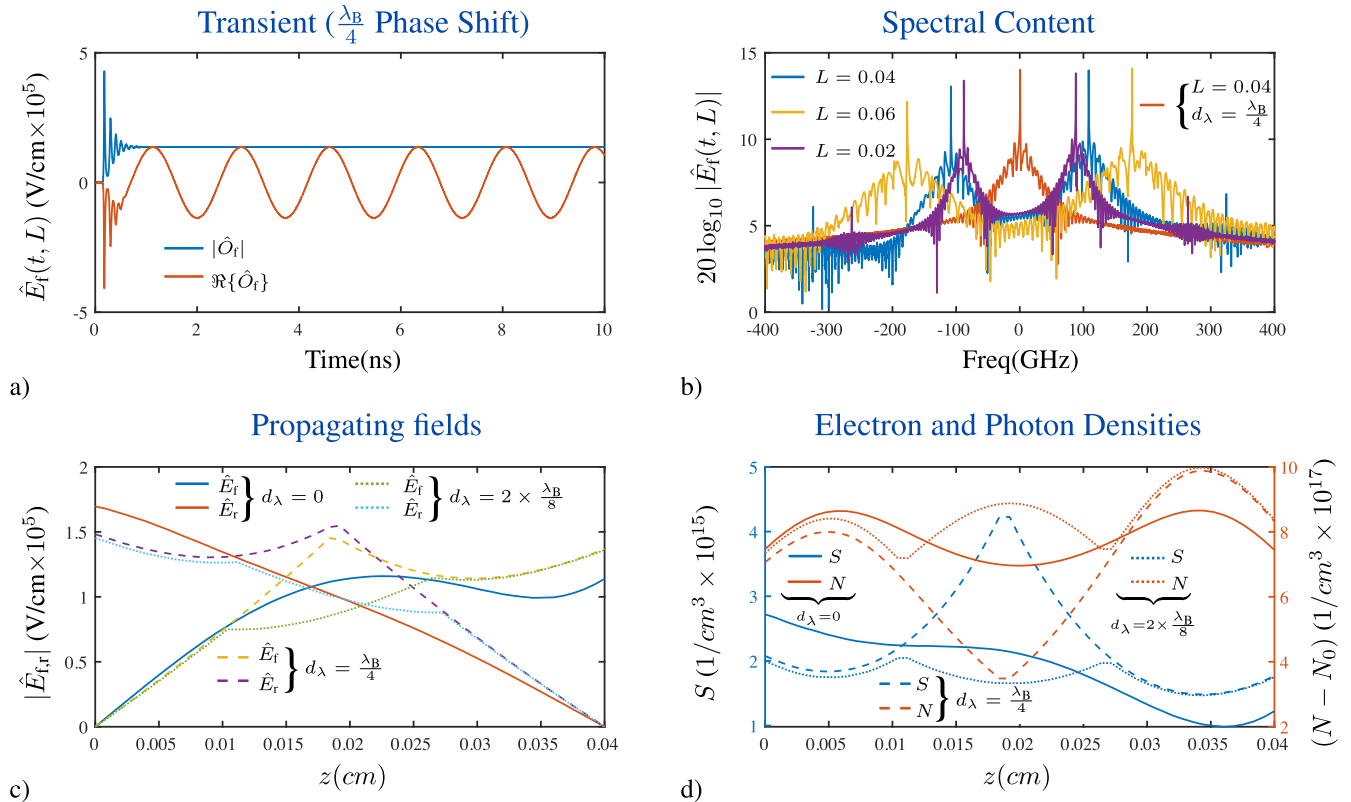
1) LASER OPERATING POINT DETERMINATION

An illustration of the use of the procedure given in Sec. III-B3 to create a laser OP is shown in Fig. 15. This figure verifies the effectiveness of creating an OP for both DFB and DBR lasers. By using the FSS to produce an approximate OP and then using the FTSS to create a final OP, simulation start-up time is greatly reduced. In these examples both DBR and DFB lasers have no delay elements present and produce an output modulated at $\Delta\omega$. The magnitude of the output is plotted in Fig. 15a, presenting both a simulation of full transient to harmonic SS over 50 ns, and a simulation started from an OP. When the laser is started from off, the initial transient is clearly seen in the first 10-20 ns. The simulation started from an OP has no appreciable transient at start-up.

Details of the harmonic SS obtained by both a full transient simulation and from an OP are presented in Fig. 15b with the optical output and average carrier density N_a plotted for both lasers. For the simulation from off, a nanosecond at the end of a 100 ns simulation is plotted. while for the simulation from an OP, the first nanosecond is presented. As can be seen for both lasers, the constructed OP is essentially identical to that of the one obtained by performing a full simulation, with both the average value and the stochastic variation well produced. The variation in the field and carrier density is due to the SPE.

---

[11]For the DFB the uniform nature of the device allows for an approximate value for the frequency shift $\Delta\omega$ to be found from the relationships: $|\beta_e L| \approx \pi/2$ with $\beta_e = \mp\sqrt{(\delta + jG_0)^2 - \hat{\kappa}^2}$ and $\delta = \Delta\omega/v_g$, where g is the net gain in the laser [20].

FIGURE 14. DFB laser full transient simulation: a) Temporal response of a laser with $\frac{\lambda_B}{4}$ grating shift. b) Spectral response showing three lengths: $L = 0.02, 0.04, 0.06$ with no grating shift and $L = 0.04$ and a $\frac{\lambda_B}{4}$ grating shift. c) Field magnitudes. d) Electron and photon densities for $L = 0.04$ and $d_\lambda = 0, \frac{\lambda_B}{4}, 2 \times \frac{1}{8}\lambda_B$.

Finally, the spectral content of the OPs for both lasers are presented in the Fig. 15c. As mentioned, both lasers do not have any delay elements and the offset from the Bragg (and implicitly the carrier frequency) is obvious. There are, of course, two possible modes at $\omega_B \pm \Delta\omega$ for the simulation from off with the dominant mode being randomly produced. For the OP simulation the mode can be chosen by construction and here was chosen to match the full simulation from off.

The sequential use of the FSS and the FTSS was found to be very effective at finding an OP for both grating-based lasers. When finding a circuit-level OP, the use of the FTSS is precluded from the initial iterations due to the need to perform a relatively large number of them. The FSS, however, is fast and deterministic so may be included in these initial iterations. Therefore the procedure proposed in [16] for use in a circuit simulator is very appropriate. During the initial stage of convergence the FSS is used. Once a circuit-level OP has been found that is consistent with the FSS, the procedure can be continued for a small number of iterations using the FTSS giving a final OP appropriate to start a transient solution.

2) DFB LASER CIRCUIT EXAMPLES

Two examples of the using a TWM-based laser compact model will be presented in order to explore system-level issues. Both examples will use a DFB laser. The first example is the simulation of a full transient from off. This example will be used to illuminate the use of detuning to remove the high frequency modulation of $\Delta\omega$ present for a laser with no delay elements as well as to discuss the bandwidth restriction present on the output of the laser model. The second example will deal with a directly modulated DFB laser driving an optical link. This example will demonstrate the model's ability to incorporate optical feedback and address the impact of the model on the stability of the simulation.

3) CIRCUIT SIMULATION OF LASER TRANSIENTS

Fig. 16 presents a comparison between the stand-alone (internal) model predictions and the TWM compact model (external) output. In the top panel we see the output field for the first nanosecond of the internal TWM output ($\hat{E}_f(t, L)$) and the external model output $\hat{O}_f(t)$. The internal output has a step-size of $\Delta t = 0.1$ ps whereas the external output is discretized by the system step-size $\Delta t_S = 1$ ps. This very fine system-level step-size is needed due to the $\Delta\omega = 108$ GHz modulation of the envelope which has an implicit carrier of ω_B. The detail on the right side of this panel shows the harmonic SS obtained at the end of a 50 ns simulation and the discretization of the model output $\hat{O}_f$ due the system-level time-step. This is an important consequence of the laser
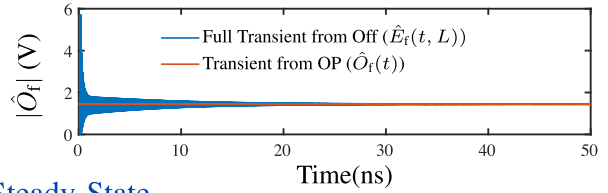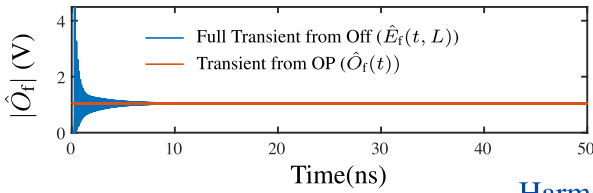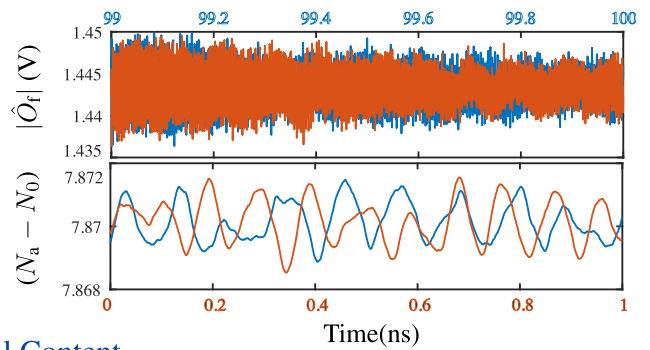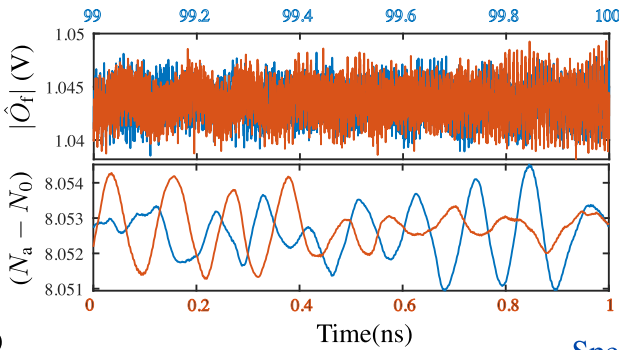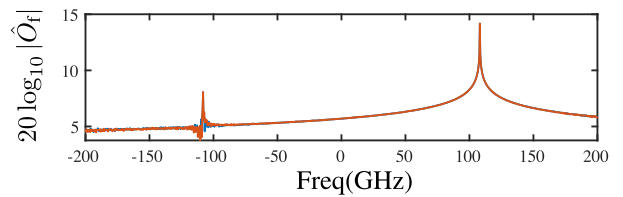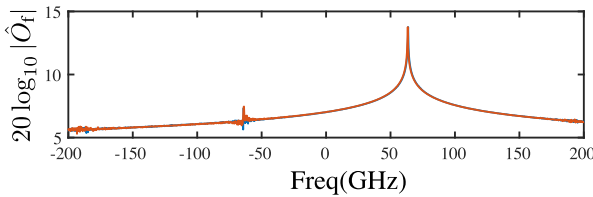
FIGURE 15. Comparison of simulation from off with an OP for both DBR and DFB lasers with zero grating shift: a) Temporal response of the optical output over 50 ns. b) Detail of optical output and average carrier density in the laser for 1 ns. For the simulation from off, a nanosecond at the end of a 100 ns simulation is used. For the simulation from an OP the first nanosecond is presented. c) Spectral response taken over 1 ns.

model as it is, being a nonlinear device, able to internally generate high frequencies which are not limited to the bandwidth of the inputs. This high internal bandwidth will typically be restricted by the interpolation process using to generate the model outputs.

The presence of this high frequency envelope modulation is undesirable from a system simulation perspective due to the need to have very small time-steps. In Fig. 16b an approach to alleviate this issue is presented. Two simulations are shown. In one case the laser has a single $\lambda_B/4$ delay element present. For this case the lasing frequency is shifted down to the implicit carrier frequency of ω_B and the envelope has no high frequency modulation present. In the second case there is no delay element present but the detuning parameter δ is set to $\Delta\omega/v_g$, implicitly moving the carrier to $\omega_B + \Delta\omega$ and removing the high frequency modulation of the envelope. As can be seen for both simulations the use of much larger system step-size of 20 ns is now appropriate.

The bottom plot in this figure presents details of the initial transient and harmonic SS for the device with a delay present. It can be seen that the 20 ps system step-size is just adequate for resolving the initial transient and very appropriate for use

at harmonic SS. A circuit simulator with a variable time-step methodology would be appropriate in this situation.
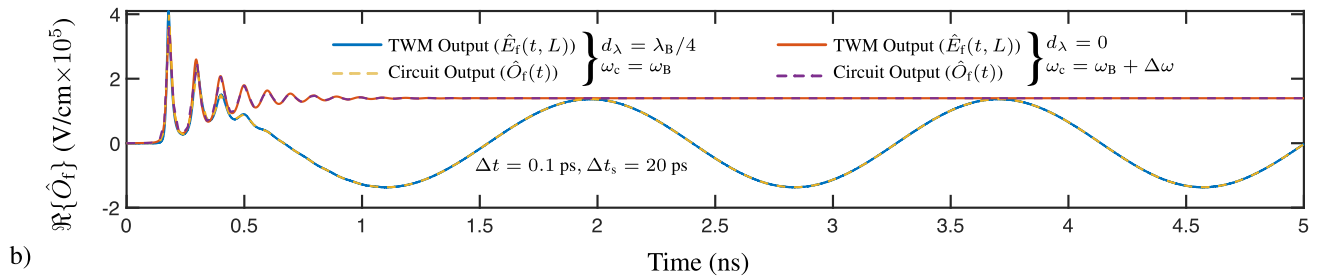
4) CIRCUIT SIMULATION OF A DIRECTLY MODULATED LASER

The second circuit example is shown in Fig. 17 and is an *OptiSPICE* simulation of a simple optical link created from a directly-modulated DFB laser, a waveguide element, a photo-detector (PD), and a low noise amplifier (LNA). A TWM compact model is used for the laser. The waveguide simply connects the laser to the photo-detector. The model of the photo-detector is an output voltage given by $V_{PDF} = \alpha_{PD}|\hat{O}_{PD}|^2$, where $\hat{O}_{PD}$ is the optical input signal to the photo-detector and α_{PD} characterises the response. The LNA is modeled by a voltage gain with a low pass filter response. Incorporated into the model is a reflected optical signal from the PD given by R_{PD}, the reflected power level. A key point of this circuit is that it is inherently nonlinear (due to the laser dynamics and output voltage of the PD being related to the square of the optical field input) and also has a feedback path which returns light back to the laser. Both of these conditions
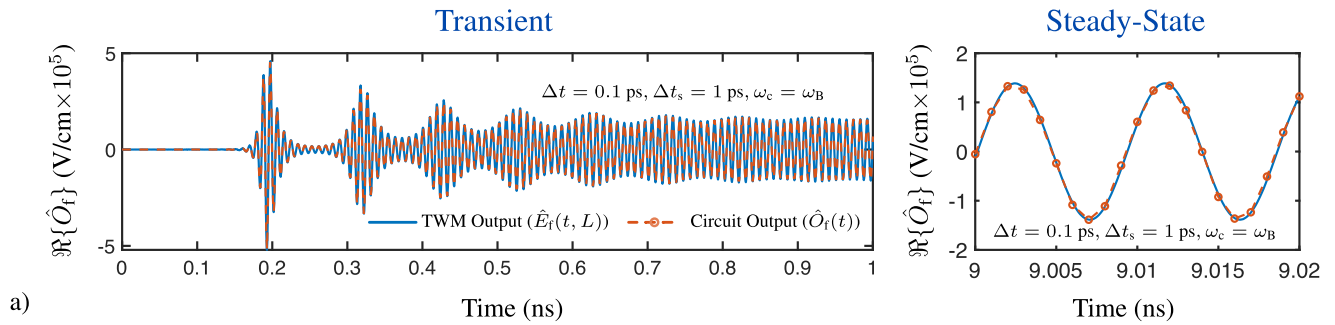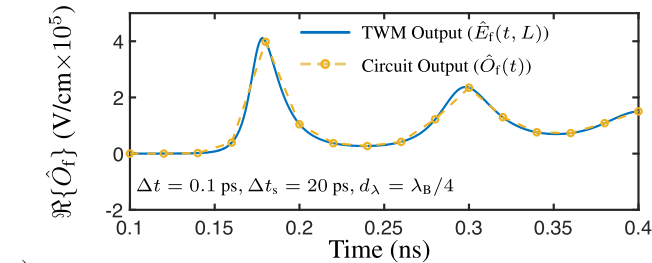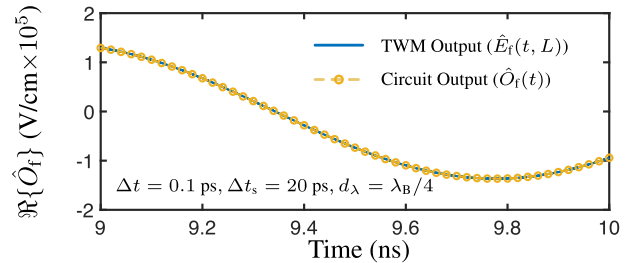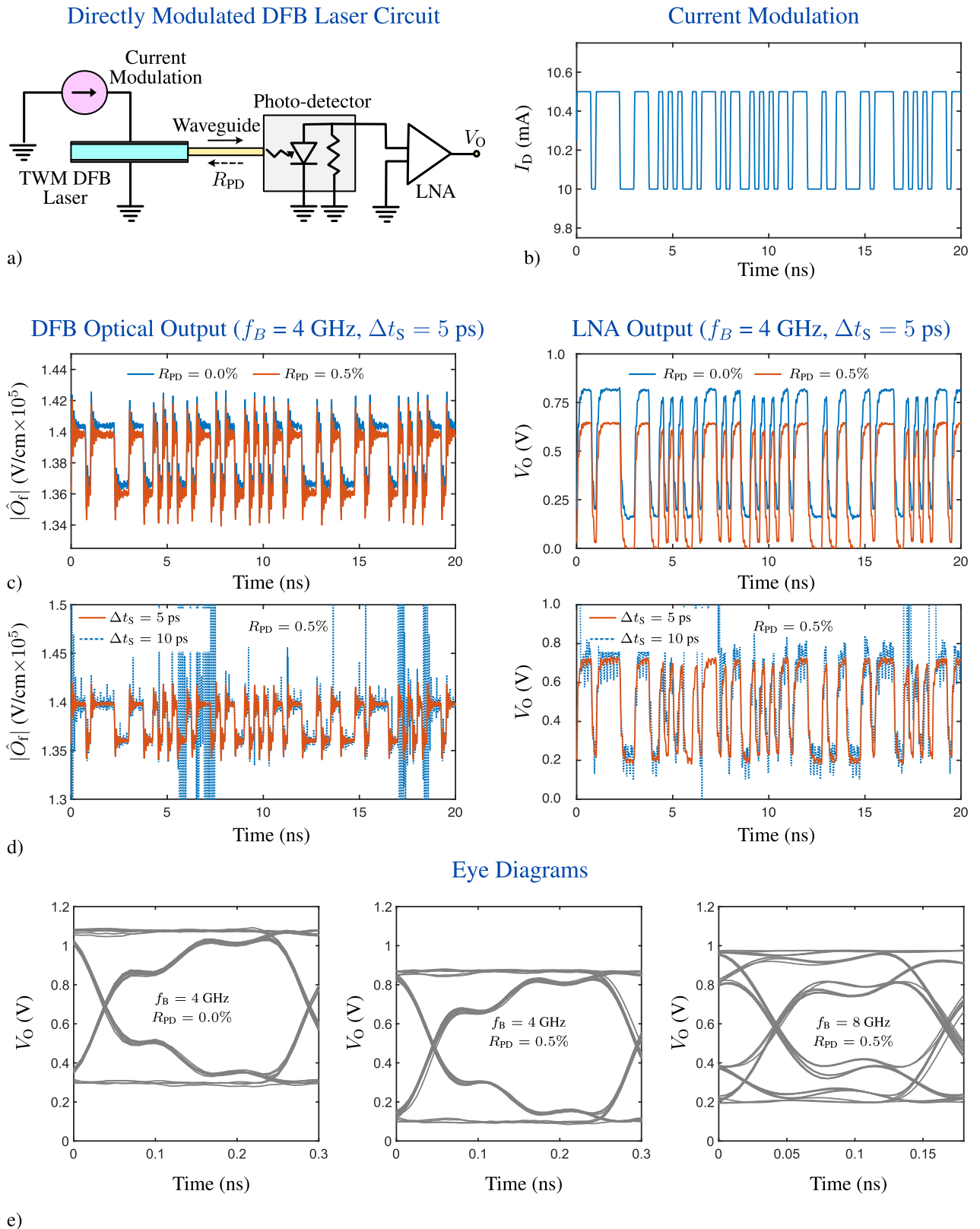
FIGURE 16. Circuit simulation of DFB laser transients. In all plots both the internal TWM and the circuit (external) output fields are shown. a) Default laser with no delay elements. Shown are two plots of the output field; one of a 1 ns transient from off and the other of the SS obtained after 9 ns. The carrier frequency is chosen to be the Bragg frequency and the circuit simulation step-size required is $\Delta t_S = 1$ ps. b) Two lasers for which the laser output frequency is near the carrier frequency: Firstly, a laser with a $\lambda_B/4$ delay and $\omega_c = \omega_B$. Secondly, a laser with no delay but where ω_c has been shifted by $\Delta \omega = 107$GHz to the laser output frequency using the detuning parameter δ. See (2). The circuit simulation step-size required is $\Delta t_S = 20$ ps. c) Details of the initial transient and harmonic SS for the device with a delay present.

require the simulator to find a self-consistent dynamic solution.

An initial 20 ns simulation was done for a current modulation prescribed by a pseudo-random 4 GHz bit stream (Fig. 17b) with a system time-step of 5 ps and no back reflection. Both the laser optical output and the LNA output are shown in Fig. 17c. The characteristic laser dynamics are evident at the bit transitions which are in large part removed by the filtering of the LNA. Also shown in these plots are the response of the circuit when the reflected power is 0.5%. The second simulation is very similar to the first but has, however, slightly smaller power levels due to a reduced gain in the laser. The voltage swing of the LNA as the bits switch is essentially unchanged. The system step-size for both simu-

lations is set to 5 ps which easily resolves the transients at the bit transitions. It is tempting to increase this step-size to facilitate faster simulations, but this can lead to stability issues.

It was found that for zero back reflection system step sizes up to at least 20 ps produced stable and accurate results. However, the introduction of a back reflection was found to create instabilities at larger system step sizes. This is illustrated in Fig. 17d where two simulations are shown for $R_{PD} = 0.5\%$. When a step-size of 5 ps is used, the simulation is stable. Increasing the step-size to 10 ps created instability and unphysical results as seen in the plot. This instability is not surprising as the dynamics of a laser with external feedback are very complex—restricting the bandwidth of the

FIGURE 17. Circuit simulation of DFB laser bit-stream at 4GHz and 8GHz. a) Circuit schematic. b) Current modulation at 4GHz. c) Comparison of circuit response with 0 and 5% optical power reflection off photo-detector. d) Response for two different system step sizes of 5 and 10 ps. e) Eye diagrams for zero reflected power at 4GHz and 0.5% reflected power for 4 and 8 GHz.

external feedback by increasing the system step-size will have effects that are hard to anticipate.

Finally, in the bottom panel of the figure, eye diagrams are presented for the LNA output for three cases. Simulations are shown for a 4 GHz bit stream, with and without reflection, and for an 8 GHz bit stream with reflection. As can be seen for this particular laser configuration the eye is starting to close as the bit rate is doubled.

VI. CONCLUSION

This paper has presented the development and use of a TWM for waveguide-based grating devices. Both passive and active devices are modeled with the grating being characterized by coupling coefficients for the two counter-propagating waves. A key feature of the TWM model is the presence of an implicit carrier and it is natural to assume this carrier is at the Bragg frequency of the grating. However, many situations occur when it would be more useful to have the carrier different from the Bragg frequency. It is shown how this can be accommodated by two methods: either by the static detuning of the TWM or introducing a phase modulation into the coupling coefficients. Other physical aspects of the model are addressed such as dispersion and energy conservation. Comparison to a 1D Yee-cell model is used to verify the applicability of the TWM. As an example of the circuit simulation of a passive device, an optical code generating application is used. This example uses the TWM compact model within the *OptiSPICE* framework to model generation of a picosecond optical code from a single incident pulse. It clearly shows that the framework proposed in [14], where the internal clock of the TWM is left undisturbed by the system-level simulation, is effective. It is also noted that for a passive device the interface between the compact model and the circuit simulator (which can produce a bandwidth restriction) is not a concern.

Using TWM-based laser simulations of DBR and DFB structures it is shown that the model captures the complex behaviour the devices. In particular, the lasing frequency is naturally produced from the model and the introduction of delay elements into the structure can be used to restrict the laser to single mode operation.

A number of examples are used to illustrate important aspects of use of the TWM as a compact model. Firstly, it is shown that a modified version of the procedure presented in [16] can be used to obtain an operating point for either of the laser configurations. A significant issue with the simulation of both laser configurations is that, if not designed with delay elements, the laser operating frequency will be of the order of a 100 GHz off the Bragg frequency (which is also implicitly the carrier frequency). This will result in the need for a very short system-level time-step. It is shown how detuning can be used (by moving the carrier frequency to the lasing frequency) to produce an unmodulated output, allowing for much more efficient simulations. The final example uses a directly-modulated DFB laser to illustrate the effect of back reflection on the stability of the laser simulation. This

example shows how the introduction of this optical feedback requires a shorter system-level time-step to produce a stable simulation.

This work shows that the methodologies presented in [14] and [16] can be used as a framework for incorporating grating based devices in a spice-like simulator. A key insight is the impact of the choice of the carrier frequency for DFB and DBR configurations on simulation efficiency. In conclusion, this paper has presented a method of incorporating TWM model of grating-based structures that is physically-based, flexible and remarkably effective.

APPENDIX A TRAVELING WAVE MODEL DERIVATION AND SPECIFICATION OF κ FOR $\omega_B \neq \omega_c$

In this section we will determine the relationship between the TWM wave coupling parameter $\hat{\kappa}$ and a cosine grating. The starting point is the 2st-order scalar wave equation describing a propagating waveguide mode characterized by a group velocity of v_g. Adding a cosine perturbation in the permittivity prescribed by Δ_ϵ we have,

$$\frac{\partial^2 \hat{E}}{\partial z^2} - \frac{1}{v_g^2}(1 + \Delta_\epsilon \cos(2k_B z))\frac{\partial^2 \hat{E}}{\partial t^2} = 0.$$

The solution can be expressed as consisting of a forward and backward traveling wave,

$$\hat{E} = \hat{E}_f(t, z)\hat{u}(x, y)e^{j(\omega_c t - k_c z)} + \hat{E}_r(t, z)\hat{u}(x, y)e^{j(\omega_c t + k_c z)},$$

with a transverse mode profile given by $\hat{u}(x, y)$, which we can absorb into $\hat{E}_f$ and $\hat{E}_r$,

$$\hat{E} = \hat{E}_f e^{j(\omega_c t - k_c z)} + \hat{E}_r e^{j(\omega_c t + k_c z)}.$$

Substitution of this ansatz and the use of Euler's identity for the cosine, a slowly varying approximation and defining $k_B = k_c + \Delta k$ we obtain the simplification

$$k_c\left(\frac{\partial \hat{E}_r}{\partial z}fe^{j(\omega_c t + k_c z)} - \frac{\partial \hat{E}_f}{\partial z}e^{j(\omega_c t - k_c z)}\right)$$

$$-\frac{\omega_c}{v_g^2}\left(\frac{\partial \hat{E}_f}{\partial t}e^{j(\omega_c t - k_c z)} - \frac{\partial \hat{E}_r}{\partial t}e^{j(\omega_c t + k_c z)}\right) =$$

$$-\frac{\Delta_\epsilon k_c^2}{4j}\left(\hat{E}_f e^{j(\omega_c t + k_c z + 2\Delta k z)} + \hat{E}_r e^{j(\omega_c t + 3k_c z + 2\Delta k z)}\right)$$

$$-\frac{\Delta_\epsilon k_c^2}{4j}\left(\hat{E}_f e^{j(\omega_c t - 3k_c z - 2\Delta k z)} + \hat{E}_r e^{j(\omega_c t - k_c z - 2\Delta k z)}\right).$$

This can be split into two equations for forward and reverse traveling components,

$$\frac{\omega_c}{v_g^2}\frac{\partial \hat{E}_f}{\partial t}e^{j(\omega_c t - k_c z)} + k_c\frac{\partial \hat{E}_f}{\partial z}e^{j(\omega_c t - k_c z)} =$$

$$\frac{\Delta_\epsilon k_c^2}{4j}\left(\hat{E}_f e^{j(\omega_c t - 3k_c z - 2\Delta k z)} + \hat{E}_r e^{j(\omega_c t - k_c z - 2\Delta k z)}\right)$$

$$\frac{\omega_c}{v_g^2}\frac{\partial \hat{E}_r}{\partial t}e^{j(\omega_c t + k_c z)} - k_c\frac{\partial \hat{E}_r}{\partial z}e^{j(\omega_c t + k_c z)} =$$
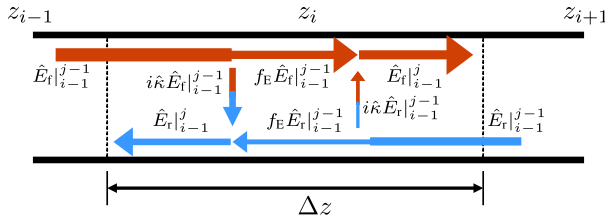
FIGURE 18. Field coupling in the TWM with energy conservation for a single spatial cell over a single time-step. The model includes the factor f_E used to correct the energy imbalance. The time index is indicated by the superscript and the spatial index by the subscript: for example $\hat{E}_f(t_{j-1}, z_{i-1}) = \hat{E}_f|_{i-1}^{j-1}$.

$$\frac{\Delta_\epsilon k_c^2}{4j} \left(\hat{E}_f e^{j(\omega_c t + k_c z + 2\Delta kz)} + \hat{E}_r e^{j(\omega_c t + 3k_c z + 2\Delta kz)} \right).$$

Imposing a phase-matching condition the $\pm 3k_c z$ terms can be removed and cancelling the common exponential factors we obtain,

$$\frac{1}{v_g} \frac{\partial \hat{E}_f}{\partial t} + \frac{\partial \hat{E}_f}{\partial z} = -jk\hat{E}_r e^{-j2\Delta kz}$$

$$\frac{1}{v_g} \frac{\partial \hat{E}_r}{\partial t} - \frac{\partial \hat{E}_r}{\partial z} = -jk\hat{E}_f e^{j2\Delta kz},$$

with $\kappa = \Delta_\epsilon k_c/4$. For $k_c = k_B$ the wave coupling is simply described by κ as shown in [20]. However, if the frequency of the carrier is such that $k_c \neq k_B$ then an additional factors of $\exp(\pm j2\Delta kz)$ must be incorporated into the TWM equations. If the grating is chirped (a non-uniform grating spacing) this can be accommodated by simply letting Δk be a function of z.

APPENDIX B TRAVELING WAVE MODEL OF A GRATING WITH ENERGY CONSERVATION

To show the need for an energy conservation correction in the simple TWM equations for a passive grating we start with (3), and assume steady-state and an index grating described by $\hat{\kappa}_f = \hat{\kappa}_r = \hat{\kappa}$ and only introduce a f_E correction factor to be determined,

$$\hat{E}_f(t_j, z_i) = f_E \hat{E}_f(t_{j-1}, z_{i-1}) + i\Delta z\hat{\kappa}\hat{E}_r(t_{j-1}, z_{i+1})$$

$$\hat{E}_r(t_j, z_i) = f_E \hat{E}_r(t_{j-1}, z_{i+1}) + i\Delta z\hat{\kappa}\hat{E}_f(t_{j-1}, z_{i-1}).$$

Fig. 18 shows the energy flow through a single cell of the TWM. We can write as the total energy $\mathcal{E}$ at t_{j-1} for adjacent cells as,

$$\mathcal{E}(t_{j-1}) = \left(|\hat{E}_f(t_{j-1}, z_{i-1})|^2 + |\hat{E}_r(t_{j-1}, z_{i+1})|^2 \right) \Delta z,$$

and we obtain,

$$\mathcal{E}(t_{j-1}) = (f_E^2 + |\Delta z\hat{\kappa}|^2)|\hat{E}_f(t_{j-1}, z_{i-1})|^2 \Delta z +$$
$$(f_E^2 + |\Delta z\hat{\kappa}|^2)|\hat{E}_r(t_{j-1}, z_{i+1})|^2)\Delta z.$$

The total energy at in the cell of interest at the next time-step t_j due to flow from adjacent cells is,

$$\mathcal{E}(t_j) = |f_E \hat{E}_f(t_{j-1}, z_{i-1}) + i\Delta z\hat{\kappa}\hat{E}_r(t_{j-1}, z_{i+1})|^2 \Delta z +$$

$$|f_E \hat{E}_r(t_{j-1}, z_{i+1}) + i\Delta z\hat{\kappa}\hat{E}_f(t_{j-1}, z_i)|^2 \Delta z,$$

which can be shown to be,

$$\mathcal{E}(t_j) = f_E^2 + |\Delta z\hat{\kappa}|^2|\hat{E}_f(t_{j-1}, z_{i-1})|^2 \Delta z +$$
$$(f_E^2 + |\Delta z\hat{\kappa}|^2)|\hat{E}_r(t_{j-1}, z_{i+1})|^2 \Delta z,$$

Conservation of energy implies $\mathcal{E}(t_j) = \mathcal{E}(t_{j-1})$ and equating the coefficients of the fields gives,

$$f_E = \sqrt{1 - |\Delta z\hat{\kappa}|^2},$$

which will be close to 1 for small Δz.

APPENDIX C DISPERSION RELATIONSHIP AND GROUP VELOCITY: 2nd-ORDER WAVE EQUATION

To determine the effective group velocity with in a grating we need to obtain the dispersion relationship for the cosine grating. As in App. A we start with a 2st-order scalar wave equation describing a propagating waveguide mode with a cosine perturbation of the permittivity,

$$\frac{d^2\hat{E}}{dz^2} - \frac{1}{v_g^2}(1 - \Delta_\epsilon \cos(2k_B z))\frac{d^2\hat{E}}{dt^2} = 0.$$

Assuming an infinite and periodic grating an appropriate solution for the problem is a Floquet-Bloch description [35],

$$\hat{E} = \sum_{n=-\infty}^{\infty} \hat{E}_n e^{j(\omega_c t - nk_B z)} e^{j\hat{K}z}, \tag{16}$$

where $\hat{K}$ is associated with a reciprocal lattice vector.

The substitution of the assumed solution and the use of Euler's identity results in,

$$\sum_{n=-\infty}^{\infty} \left(v_p^2(\hat{K} - nk_B)^2 - \omega_c^2 \right) \hat{E}_n e^{-jnk_B z} +$$

$$\sum_{n=-\infty}^{\infty} \omega_c^2 \frac{\Delta_\epsilon}{2} \hat{E}_{n+2} e^{-jnk_B z} + \sum_{n=-\infty}^{\infty} \omega_c^2 \frac{\Delta_\epsilon}{2} \hat{E}_{n-2} e^{-jnk_B z} = 0,$$

matching powers of $e^{jnk_B z}$ due to the orthogonality of the terms in the expansion we obtain,

$$\Gamma_n \hat{E}_n + \omega_\Delta \hat{E}_{n+2} + \omega_\Delta \hat{E}_{n-2} = \Lambda_n \hat{K}\hat{E}_n - v_p^2 \hat{K}^2 \hat{E}_n,$$

with,

$$\Gamma_n = v_p^2(n^2 k_B^2) - \omega_c^2, \quad \omega_\Delta = \omega_c^2 \frac{\Delta_\epsilon}{2}, \quad \Lambda_n = 2 v_p^2 nk_B.$$

This equation couples the coefficients of the Bloch Solution (16) and by limiting the number of terms in the solution to $2N + 1$ where $\pm N$ are the limits on the expansion a matrix equation can be formed,

$$\mathbf{G}\hat{\mathbf{E}} = \hat{K}L\hat{\mathbf{E}} - v_p^2 \hat{K}^2 \mathbf{I}\hat{\mathbf{E}},$$

with

$$\mathbf{G} = \begin{bmatrix} \Gamma_{-N} & 0 & \Omega_\Delta & 0 & \cdots & & \\ 0 & \Gamma_{-N+1} & 0 & \Omega_\Delta & 0 & \cdots & \\ \Omega_\Delta & 0 & \Gamma_{-N+2} & 0 & \Omega_\Delta & 0 & \cdots \\ \vdots & \ddots & \ddots & \ddots & \ddots & \ddots & \vdots \\ 0 & \cdots & \Omega_\Delta & 0 & \Gamma_{N-2} & 0 & \Omega_\Delta \\ 0 & \cdots & & 0 & \Omega_\Delta & 0 & \Gamma_{N-1} & 0 \\ 0 & \cdots & & \cdots & 0 & \Omega_\Delta & 0 & \Gamma_N \end{bmatrix}$$

$$\mathbf{E} = \begin{bmatrix} \hat{E}_{-N} & \hat{E}_{-N+1} & \cdots & \hat{E}_0 & \cdots & \hat{E}_{N-1} & \hat{E}_N \end{bmatrix}^{\mathrm{T}}$$

$$\mathbf{L} = \begin{bmatrix} \Lambda_{-N} & 0 & \cdots \\ \vdots & \ddots & \cdots \\ 0 & \cdots & \Lambda_N \end{bmatrix} \quad \text{and} \quad \mathbf{I} = \begin{bmatrix} 1 & 0 & \cdots \\ \vdots & \ddots & \cdots \\ 0 & \cdots & 1 \end{bmatrix}.$$

This is a nonlinear Eigenvalue equation, however, it can be linearized by a simple substitution,

$$\hat{\mathbf{E}}_{\mathbf{f}} = \hat{K}\hat{\mathbf{E}}$$
$$\mathbf{G}\hat{\mathbf{E}} = \hat{K}\mathbf{L} - v_p^2 \mathbf{I}\hat{\mathbf{E}}_{\mathbf{f}},$$

and we can write,

$$\begin{bmatrix} \varnothing & \mathbf{I} \\ \mathbf{G} & \varnothing \end{bmatrix} \begin{bmatrix} \hat{\mathbf{E}} \\ \hat{\mathbf{E}}_{\mathbf{f}} \end{bmatrix} = \hat{K} \begin{bmatrix} \mathbf{I} & \varnothing \\ \mathbf{L} & -v_p^2\mathbf{I} \end{bmatrix} \begin{bmatrix} \hat{\mathbf{E}} \\ \hat{\mathbf{E}}_{\mathbf{f}} \end{bmatrix},$$

which gives,

$$\mathbf{A}\Psi = \hat{K}\mathbf{B}\Psi$$

, which is generalized linear eigenvalue problem.

Solution of this equation for a specific ω_c value will provide a set of $\hat{K}$ eigenvalues. If the $\hat{K}$ eigenvalue is real the mode propagates, whereas complex $\hat{K}$ implies an evanescent mode and the presence of a stop-band. Using this equation a dispersion relationship ω_c versus $\hat{K}$ can be obtained by simply solving over a range of ω_c values and determining $\hat{K}$. The effective velocity of signals in the grating can be determined from $v_g'(\omega_c) = d\omega_c / d\hat{K}$.

APPENDIX D DISPERSION RELATIONSHIP AND GROUP VELOCITY: TRAVELING WAVE EQUATIONS

A 1st-order dispersion relationship can be obtained directly from the TWM equations. Following the procedure given in [28] we start with the TWM equations for a grating,

$$\frac{1}{v_g}\frac{\partial \hat{E}_{\mathrm{f}}}{\partial t} = -\frac{\partial \hat{E}_{\mathrm{f}}}{\partial z} + i\hat{\kappa}\hat{E}_{\mathrm{r}}$$
$$\frac{1}{v_g}\frac{\partial \hat{E}_{\mathrm{r}}}{\partial t} = +\frac{\partial \hat{E}_{\mathrm{r}}}{\partial z} + i\hat{\kappa}\hat{E}_{\mathrm{f}}.$$

Defining a detuning factor,

$$\delta = \frac{\omega_c - \omega_{\mathrm{B}}}{v_g},$$

and assuming a time dependence of $\exp(i\delta v_g t)$ we obtain a frequency domain version of the TWM equations,

$$i\delta \hat{E}_{\mathrm{f}} = -\frac{\partial \hat{E}_{\mathrm{f}}}{\partial z} + i\hat{\kappa}\hat{E}_{\mathrm{r}}$$

$$i\delta \hat{E}_{\mathrm{r}} = +\frac{\partial \hat{E}_{\mathrm{r}}}{\partial z} + i\hat{\kappa}\hat{E}_{\mathrm{f}}.$$

A general solution to this set of equations, assuming no gain or loss, is,

$$\hat{E}_{\mathrm{f}} = \hat{f}_1 e^{iKz} + \hat{f}_2 e^{-iKz}$$
$$\hat{E}_{\mathrm{r}} = \hat{r}_1 e^{iKz} + \hat{r}_2 e^{-iKz}.$$

Substitution into TWM equations (3) produces,

$$i\delta(\hat{f}_1 e^{iKz} + \hat{f}_2 e^{-iKz}) = -(\hat{f}_1 iKe^{iKz} - \hat{f}_2 iKe^{-iKz})$$
$$+ i\kappa(\hat{r}_1 e^{iKz} + \hat{r}_2 e^{-iKz})$$
$$i\delta(\hat{r}_1 e^{iKz} + \hat{r}_2 e^{-iKz}) = (\hat{r}_1 iKe^{iKz} - \hat{r}_2 iKe^{-iKz})$$
$$+ i\kappa(\hat{f}_1 e^{iKz} + \hat{f}_2 e^{-iKz}).$$

The grating is symmetrical and we have $s_1 = r_2$ and $s_2 = r_1$, using the second equation and matching exponential terms we get two coupled equations,

$$\delta\hat{r}_1 = \hat{r}_1 K + \kappa\hat{r}_2$$
$$\delta\hat{r}_2 = -\hat{r}_2 K + \kappa\hat{r}_1.$$

An explicit solution of this is,

$$r_1 = \frac{\kappa}{\delta - K}r_2,$$

and for non-trivial solutions we have,

$$\delta^2 - K^2 = \kappa^2.$$

This equation is an explicit dispersion relationship between K and ω_c,

$$K = \frac{1}{v_g}\sqrt{(\omega_c - \omega_{\mathrm{B}})^2 - \kappa^2}.$$

Finally, we obtain a corrected group velocity,

$$v_g' = \frac{d\omega_c}{dK} = v_g\sqrt{\frac{(\omega_c - \omega_{\mathrm{B}})^2 - \kappa^2}{(\omega_c - \omega_{\mathrm{B}})^2}}.$$

REFERENCES

[1] L. M. Augustin, R. Santos, E. D. Haan, S. Kleijn, P. J. A. Thijs, S. Latkowski, and D. Zhao, "InP-based generic foundry platform for photonic integrated circuits," *IEEE J. Sel. Topics Quantum Electron.*, vol. 24, no. 1, pp. 1–10, Jan. 2018.

[2] L. Chrostowski, J. Flueckiger, C. Lin, M. Hochberg, J. Pond, J. Klein, J. Ferguson, and C. Cone, "Design methodologies for silicon photonic integrated circuits," *Proc. SPIE*, vol. 8989, Jan. 2014, Art. no. 89890G.

[3] L. Chrostowski and M. Hochberg, *Silicon Photonics Design: From Devices to Systems*. Cambridge, U.K.: Cambridge Univ. Press, 2015.

[4] Z. Zhang, R. Wu, Y. Wang, C. Zhang, E. J. Stanton, C. L. Schow, K.-T. Cheng, and J. E. Bowers, "Compact modeling for silicon photonic heterogeneously integrated circuits," *J. Lightw. Technol.*, vol. 35, no. 14, pp. 2973–2980, Jul. 15, 2017.

[5] W. Bogaerts and L. Chrostowski, "Silicon photonics circuit design: Methods, tools and challenges," *Laser Photon. Rev.*, vol. 12, no. 4, Apr. 2018, Art. no. 1700237.

[6] *OptiSpice*. [Online]. Available: http://www.optiwave.com

[7] *Lumerical Interconnect*. [Online]. Available: http://www.lumerical.com

[8] *VPIcomponentMaker*. [Online]. Available: http://www.vpiphotonics.com

[9] U. Bendelow, M. Radziunas, J. Sieber, and M. Wolfrum, "Impact of gain dispersion on the spatio-temporal dynamics of multisection lasers," *IEEE J. Quantum Electron.*, vol. 37, no. 2, pp. 183–188, Feb. 2001.

[10] R. Čiegis and M. Radziunas, "Effective numerical integration of traveling wave model for edge-emitting broad-area semiconductor lasers and amplifiers," *Math. Model. Anal.*, vol. 15, no. 4, pp. 409–430, Jan. 2010. [Online]. Available: http://www.tandfonline.com/doi/abs/10.3846/1392-6292.2010.15.409-430

[11] J. Sieber, "Numerical bifurcation analysis for multisection semiconductor lasers," *SIAM J. Appl. Dyn. Syst.*, vol. 1, no. 2, pp. 248–270, Jan. 2002, doi: 10.1137/S1111111102401746.

[12] M. Radziunas, M. Khoder, V. Tronciu, J. Danckaert, and G. Verschaffelt, "Semiconductor ring laser with filtered optical feedback: Traveling wave description and experimental validation," *J. Opt. Soc. Amer. B, Opt. Phys.*, vol. 35, no. 2, pp. 380–390, Feb. 2018. [Online]. Available: http://josab.osa.org/abstract.cfm?URI=josab-35-2-380

[13] J. Piprek, *Handbook of Optoelectronic Device Modeling and Simulation: Lasers, Modulators, Photodetectors, Solar Cells, and Numerical Methods* (Series in Optics and Optoelectronics). Boca Raton, FL, USA: CRC Press, 2017. [Online]. Available: https://books.google.ca/books?id=MGpQDwAAQBAJ

[14] T. Smy and J. H. Rasmussen, "Integration of traveling wave optical device models into an MNA-based circuit simulator," *IEEE Trans. Comput.-Aided Design Integr. Circuits Syst.*, vol. 39, no. 12, pp. 4338–4350, Dec. 2020.

[15] M. Sciamanna and K. A. Shore, "Physics and applications of laser diode chaos," *Nature Photon.*, vol. 9, no. 3, p. 151, 2015.

[16] J. H. Rasmussen and T. J. Smy, "Obtaining an operating point solution of a traveling wave laser model," *IEEE Access*, vol. 9, pp. 54775–54795, 2021.

[17] M. A. Butt, N. L. Kazanskiy, and S. N. Khonina, "Advances in waveguide Bragg grating structures, platforms, and applications: An up-to-date appraisal," *Biosensors*, vol. 12, no. 7, p. 497, 2022. [Online]. Available: https://www.mdpi.com/2079-6374/12/7/497

[18] M. Burla, L. R. Cortés, M. Li, X. Wang, L. Chrostowski, and J. Azaña, "Integrated waveguide Bragg gratings for microwave photonics signal processing," *Opt. Exp.*, vol. 21, no. 21, pp. 25120–25147, 2013. [Online]. Available: https://opg.optica.org/oe/abstract.cfm?URI=oe-21-21-25120

[19] H. Saghaei, P. Elyasi, and B. J. Shastri, "Sinusoidal and rectangular Bragg grating filters: Design, fabrication, and comparative analysis," *J. Appl. Phys.*, vol. 132, no. 6, Aug. 2022, Art. no. 064501, doi: 10.1063/5.0098923.

[20] J. Carroll, J. Whiteaway, and D. Plumb, *Distributed Feedback Semiconductor Lasers*. Bellingham, WA, USA: SPIE, 1998.

[21] A. Perez-Serrano, M. Vilera, J. M. G. Tijero, S. Balle, and I. Esquivias, "A voltage driven traveling-wave model for the simulation of an integrated three-section MOPA under static and modulated operation," *IEEE J. Quantum Electron.*, vol. 54, no. 2, pp. 1–10, Apr. 2018.

[22] C. Z. Ning, R. A. Indik, and J. V. Moloney, "Effective Bloch equations for semiconductor lasers and amplifiers," *IEEE J. Quantum Electron.*, vol. 33, no. 9, pp. 1543–1550, Sep. 1997.

[23] P. Gunupudi, T. Smy, J. Klein, and Z. J. Jakubczyk, "Self-consistent simulation of opto-electronic circuits using a modified nodal analysis formulation," *IEEE Trans. Adv. Packag.*, vol. 33, no. 4, pp. 979–993, Nov. 2010.

[24] C.-W. Ho, A. Ruehli, and P. Brennan, "The modified nodal approach to network analysis," *IEEE Trans. Circuits Syst.*, vol. CS-22, no. 6, pp. 504–509, Jun. 1975.

[25] T. Quarles, A. Newton, D. Pederson, and A. Sangiovanni-Vincentelli, "SPICE 3 version 3F5 user's manual," Dept. EECE, Univ. California, Berkeley, CA, USA, Tech. Rep., 1994.

[26] C. Bonfil, T. Smy, and P. Weetmen, "Integration of traveling wave laser model into an mixed electrical/optical circuit simulator," in *Proc. IEEE Opt. Interconnects Conf. (OI)*, Apr. 2015, pp. 88–89.

[27] A. Yariv, "Coupled-mode theory for guided-wave optics," *IEEE J. Quantum Electron.*, vol. QE-9, no. 9, pp. 919–933, Sep. 1973.

[28] H. Kogelnik and C. V. Shank, "Coupled-wave theory of distributed feedback lasers," *J. Appl. Phys.*, vol. 43, no. 5, pp. 2327–2335, May 1972, doi: 10.1063/1.1661499.

[29] R. Cheng, N. A. F. Jaeger, and L. Chrostowski, "Fully tailorable integrated-optic resonators based on chirped waveguide Moiré gratings," *Optica*, vol. 7, no. 6, pp. 647–657, Jun. 2020. [Online]. Available: https://opg.optica.org/optica/abstract.cfm?URI=optica-7-6-647

[30] C. J. Brooks, G. L. Vossler, and K. A. Winick, "Integrated-optic dispersion compensator that uses chirped gratings," *Opt. Lett.*, vol. 20, no. 4, pp. 368–370, Feb. 1995. [Online]. Available: https://opg.optica.org/ol/abstract.cfm?URI=ol-20-4-368

[31] A. Katzir, A. Livanos, J. Shellan, and A. Yariv, "Chirped gratings in integrated optics," *IEEE J. Quantum Electron.*, vol. QE-13, no. 4, pp. 296–304, Apr. 1977.

[32] L. M. Rivas, M. J. Strain, D. Duchesne, A. Carballar, M. Sorel, R. Morandotti, and J. Azaña, "Picosecond linear optical pulse shapers based on integrated waveguide Bragg gratings," *Opt. Lett.*, vol. 33, no. 21, pp. 2425–2427, Nov. 2008. [Online]. Available: https://opg.optica.org/ol/abstract.cfm?URI=ol-33-21-2425

[33] H. Ghafouri-Shiraz and C. Y. J. Chu, "Distributed feedback lasers: An overview," *Fiber Integr. Opt.*, vol. 10, no. 1, pp. 23–47, Jan. 1991, doi: 10.1080/01468039108201603.

[34] W. Streifer, D. Scifres, and R. Burnham, "Coupling coefficients for distributed feedback single- and double-heterostructure diode lasers," *IEEE J. Quantum Electron.*, vol. QE-11, no. 11, pp. 867–873, Nov. 1975.

[35] S. Taravati and G. V. Eleftheriades, "Generalized space-time-periodic diffraction gratings: Theory and applications," *Phys. Rev. A, Gen. Phys.*, vol. 12, no. 2, Aug. 2019, Art. no. 024026.

[36] A. Taflove and S. C. Hagness, *Computational Electrodynamics: The Finite-difference Time-Domain Method*. Norwood, MA, USA: Artech House, 2010.

[37] A. M. Weiner, "Femtosecond optical pulse shaping and processing," *Prog. Quantum Electron.*, vol. 19, no. 3, pp. 161–237, 1995. [Online]. Available: https://www.sciencedirect.com/science/article/pii/007967279400013O

[38] J. Azaña and L. R. Chen, "Synthesis of temporal optical waveforms by fiber Bragg gratings: A new approach based on space-to-frequency-to-time mapping," *J. Opt. Soc. Amer. B, Opt. Phys.*, vol. 19, no. 11, pp. 2758–2769, Nov. 2002. [Online]. Available: https://opg.optica.org/josab/abstract.cfm?URI=josab-19-11-2758

[39] A. Krishnan, L. G. de Peralta, V. Kuryatkov, A. A. Bernussi, and H. Temkin, "Direct space-to-time pulse shaper with reflective arrayed waveguide gratings and phase masks," *Opt. Lett.*, vol. 31, no. 5, pp. 640–642, Mar. 2006. [Online]. Available: https://opg.optica.org/ol/abstract.cfm?URI=ol-31-5-640

• • •